2016

Monitoring daily evapotranspiration over two California vineyards using Landsat 8 in a multi-sensor data fusion approach

Kathryn A. Semmens
USDA-ARS, kalese@gmail.com

Martha C. Anderson
USDA-ARS, martha.anderson@ars.usda.gov

William P. Kustas
USDA-ARS

Feng Gao
USDA-ARS, Feng.Gao@ars.usda.gov

Joseph G. Alfieri
USDA-ARS, joe.alfieri@ars.usda.gov

See next page for additional authors

Follow this and additional works at: https://digitalcommons.unl.edu/usdaarsfacpub

Authors

Kathryn A. Semmens, Martha C. Anderson, William P. Kustas, Feng Gao, Joseph G. Alfieri, Lynn McKee, John H. Prueger, Christopher R. Hain, Carmelo Cammalleri, Yun Yang, Tina Xia, Luis Sanchez, Maria Mar Alsina, and Monica Velez

Monitoring daily evapotranspiration over two California vineyards using Landsat 8 in a multi-sensor data fusion approach

Kathryn A. Semmens [a,*], Martha C. Anderson [a], William P. Kustas [a], Feng Gao [a], Joseph G. Alfieri [a], Lynn McKee [a], John H. Prueger [b], Christopher R. Hain [c], Carmelo Cammalleri [d], Yun Yang [a], Ting Xia [e], Luis Sanchez [f], Maria Mar Alsina [f], Mónica Vélez [g]

[a] USDA-ARS, Hydrology and Remote Sensing Laboratory, Beltsville, MD, USA
[b] USDA-ARS, National Laboratory for Agriculture and the Environment, Ames, IA, USA
[c] Earth System Science Interdisciplinary Center, University of Maryland, College Park, MD, USA
[d] European Commission Joint Research Centre, Institute for Environment and Sustainability, Climate Risk Management Unit, Italy
[e] Tsinghua University, Beijing, China
[f] E&J Gallo Winery Viticulture Research, Modesto, CA, USA
[g] University of Puerto Rico-Rio Piedras, USDA Hispanic Serving Institutions National Program, Puerto Rico

ARTICLE INFO

ABSTRACT

California's Central Valley grows a significant fraction of grapes used for wine production in the United States. With increasing vineyard acreage, reduced water availability in much of California, and competing water use interests, it is critical to be able to monitor regional water use and evapotranspiration (ET) over large areas, but also in detail at individual field scales to improve water management within these viticulture production systems. This can be achieved by integrating remote sensing data from multiple satellite systems with different spatiotemporal characteristics. In this research, we evaluate the utility of a multi-scale system for monitoring ET as applied over two vineyard sites near Lodi, California during the 2013 growing season, leading into the drought in early 2014. The system employs a multi-sensor satellite data fusion methodology (STARFM: Spatial and Temporal Adaptive Reflective Fusion Model) combined with a multi-scale ET retrieval algorithm based on the Two-Source Energy Balance (TSEB) land-surface representation to compute daily ET at 30 m resolution. In this system, TSEB is run using thermal band imagery from the Geostationary Environmental Operational Satellites (GOES; 4-km spatial resolution, hourly temporal sampling), the Moderate Resolution Imaging Spectroradiometer (MODIS) data (1 km resolution, daily acquisition) and the new Landsat 8 satellite (sharpened to 30 m resolution, ~16 day acquisition). Estimates of daily ET generated in two neighboring fields of Pinot noir vines of different age agree with ground-based flux measurements acquired in-field during most of the 2013 season with relative mean absolute errors on the order of 19–23% (root mean square errors of approximately 1 mm d^{-1}), reducing to 14–20% at the weekly timestep relevant for irrigation management (~5 mm wk^{-1}). A model overestimation of ET in the early season was detected in the younger vineyard, perhaps relating to an inter-row grass cover crop. Spatial patterns of cumulative ET generally correspond to measured yield maps and indicate areas of variable crop moisture, soil condition, and yield within the vineyards that could require adaptive management. The results suggest that multi-sensor remote sensing observations provide a unique means for monitoring crop water use and soil moisture status at field-scales over extended growing regions, and may have value in supporting operational water management decisions in vineyards and other high value crops.

Published by Elsevier Inc. This is an open access article under the CC BY-NC-ND license (http://creativecommons.org/licenses/by-nc-nd/4.0/).

1. Introduction

California, as the state producing over 90% of wine in the United States, has seen steady growth in the amount of acreage dedicated to wine-grape production with approximately 615,000 acres planted in 2014, up from 610,000 in 2013 (California Department of Food and Agriculture & USDA National Agricultural Statistics Service, 2014). Given the high value of this crop commodity, the continued growth in production, and limited water availability in the state, there is significant interest in developing efficient water management strategies for California vineyards. Of particular importance for high quality wine grapes is controlled water stress at key points during the growing season. To effectively manage water stress, adequate moisture is maintained from bud break until fruit set, followed by moderate water stress through veraison (change of color of grapes) and ripening in

* Corresponding author.
E-mail address: kalese@gmail.com (K.A. Semmens).

order to focus plant resources on fruit maturation rather than foliage expansion (Robinson, 2006). Ideally, this balancing of water stress would require daily monitoring of vineyard soil moisture status, but ground-based measurements may not always be representative of whole-field conditions and are costly to install and maintain, especially for large scale and distributed production systems. One method to efficiently assess and monitor water use and stress in vineyards is through satellite based estimation of evapotranspiration (ET), quantifying the net loss of water vapor from the crop field to the atmosphere.

ET is a major surface water balance component in semi-arid environments typical of many viticulture areas (Moussa, Chahinian, & Bocquillon, 2007). For vineyards, ET is usually modeled as a function of potential ET under unstressed conditions and vegetation cover fraction (Riou, Pieri, & Le Clech, 1994; Riou, Valancogne, & Pieri, 1989). However, more complex Soil–Vegetation–Atmosphere Transfer (SVAT) models have been developed to estimate seasonal ET and account for common soil management practices in viticulture such as the use of grass cover between rows (Montes, Lhomme, Demarty, Prevot, & Jacob, 2014). ET has been estimated for vineyards using weighing lysimeters, eddy covariance, or energy balance using the Bowen ratio but such "point measurements" are difficult to extrapolate to whole fields and basins and in-field spatial variability is missed (Teixeira, Bastiaanssen, & Bassoi, 2007). Thus, complete field-scale maps of ET can be of significant value in managing vineyards and efficiently planning irrigation schemes, particularly when implemented over extensive acreages.

Irrigation amounts at 80% of full potential ET have been found to maximize berry size for raisin and table grapes (Williams, 2001). Over-irrigation can reduce yield and compromise quality in certain grape varieties (Chaves et al., 2007; Williams, Grimes, & Phene, 2010), but there is still debate over amounts and timing of irrigation for a given environment and grape variety (Chaves et al., 2007). Regardless of the debate on application amount, it is clear that ET and water use estimates are necessary to effectively manage high productivity and quality in viticultural systems.

Land-surface temperature (LST), derived from thermal infrared (TIR) imagery acquired from satellites such as Landsat, has successfully been used to estimate ET over a range of spatial scales. This is because LST is sensitive to local moisture variations, providing valuable information on surface energy budget partitioning (Anderson, Allen, Morse, & Kustas, 2012). Several workable approaches to TIR-based ET mapping have been developed (e.g., Bastiaanssen, Menenti, Feddes, & Holtslag, 1998; Su, 2002; Allen, Tasumi, & Trezza, 2007; Anderson, Kustas, et al., 2012). Due to large uncertainties in determining absolute LST, most of these approaches use relative variability in LST, measured either temporally (time-differential methods) or spatially (end-member pixel scaling), to more accurately estimate ET. The Surface Energy Balance Algorithm for Land (SEBAL; Bastiaanssen et al., 1998) and the Mapping Evapotranspiration with Internalized Calibration (METRIC; Allen et al., 2007) are examples of approaches using TIR end-member pixels to represent limiting and non-limiting moisture conditions. The Atmosphere–Land Exchange Inverse (ALEXI; Anderson, Norman, Diak, Kustas, & Mecikalski, 1997; Anderson et al., 2007) model uses the time-differential approach, measuring the morning LST rise and relating the change to surface moisture and heat fluxes. Another approach for estimating ET, the crop coefficient approach, uses meteorological data and crop specific coefficients instead of LST (Allen, Pereira, Raes, & Smith, 1998). Crop coefficient techniques, however, do not capture short-term variability in soil moisture and vegetation stress conditions (Anderson, Allen, et al., 2012) which are important to vineyard management. Vegetation stress and soil moisture status do have a thermal signature, which is effectively exploited in energy balance approaches.

For viticultural decision making, water use information is most useful at field or sub-field scales, making the 30 m resolution of Landsat imagery particularly important. Unfortunately, the Landsat overpass frequency is often insufficient, typically with an ~16 day revisit interval

or longer if cloud cover is persistent. While there are TIR satellites that provide daily coverage (e.g., geostationary satellites, and moderate resolution polar orbiting systems like the Moderate Resolution Imaging Spectroradiometer — MODIS), these are too coarse in resolution (km-scale or larger) to provide the required field-scale information. Therefore, an integrated multi-sensor approach that combines the benefits of the high spatial resolution of Landsat and the high temporal resolution of MODIS and geostationary satellites to provide daily field-scale ET estimates may be of significant benefit to vineyard managers.

In this paper, we extend the multi-sensor ET mapping technique described by Cammalleri, Anderson, Gao, Hain and Kustas (2013, 2014) to viticultural systems and evaluate its performance in comparison with field measurements. This energy balance approach combines multi-scale and multi-temporal sharpened TIR imagery from geostationary satellites (4 km, hourly), MODIS (1 km, daily) and Landsat (30 m, ~bi-weekly to monthly) using the Spatial and Temporal Adaptive Reflectance Fusion Model (STARFM) data fusion methodology developed by Gao, Masek, Schwaller, and Hall (2006). Cammalleri et al. (2013) described initial implementation and evaluation of the ET fusion methodology over rainfed corn and soybean fields in the Walnut Creek watershed (Iowa) using flux data collected during the Soil Moisture Experiment of 2002 (SMEX02). It was subsequently tested for corn and cotton under both rainfed and irrigated management at two sites with contrasting climate conditions: a semi-arid site (part of the Bushland Evapotranspiration and Agricultural Remote sensing EXperiment 2008; BEAREX08, Evett et al., 2012) near Bushland, TX, and at a more temperate Ameriflux site near Mead, NE (Cammalleri, Anderson, Gao, et al. 2014). Both of these studies used data from Landsats 5 and 7.

This paper discusses application of the multi-scale ET data fusion system to a new kind of crop (wine grapes) grown in a Mediterranean climate, and to data collected with the new Thermal Infrared Sensor (TIRS) system on-board Landsat 8, which was launched in Feb of 2013. The vineyard architecture presents unique challenges to the Two-Source Energy Balance (TSEB) model that forms the land-surface representation in the retrieval algorithm, given the highly structured nature of the vine rows and the common practice of growing a cover crop between rows to control springtime soil moisture conditions. The data fusion algorithm was applied over a region in the California Central Valley near the city of Lodi for the 2013 growing season, and evaluated with micrometeorological data collected in two Pinot noir vineyards at different stages of maturity. The satellite-based flux retrievals are compared to eddy covariance measurements, as well as in-field soil moisture and yield data.

In Section 2 we provide a description the data fusion package, followed by a description of the study area and input and evaluation datasets in Section 3. Results and conclusions are presented in Sections 4 and 5, including planned future work.

2. Model descriptions

A schematic overview of the data fusion processing package, including inputs and image processing steps, is shown in Fig. 1. The main diagnostic input, the land surface temperature (LST), can be retrieved from various thermal imaging sensors over a range of different spatial and temporal resolutions. Remotely sensed LST inputs drive a multi-scale surface energy balance algorithm (Anderson, Kustas, et al., 2012), as described below.

2.1. ALEXI

The multi-scale energy balance modeling scheme has its foundation on coarse-scale regional flux estimates from the Atmosphere–Land Exchange Inverse (ALEXI) model, driven primarily by a diagnostic measurement of the morning rate of surface temperature rise, which can be acquired from geostationary satellites. The use of a time-differential LST measurement, rather than absolute instantaneous measurements
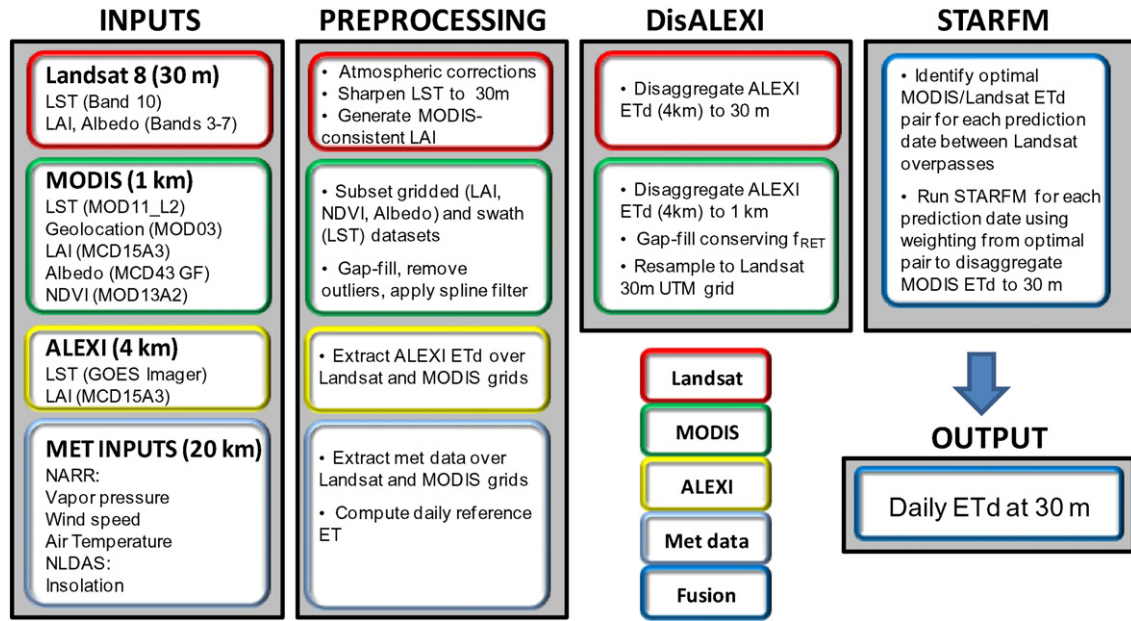
Fig. 1. Schematic overview of the inputs and processing steps in the ET data fusion system.

of LST, reduces model sensitivity to errors in temperature retrieval due to atmospheric and emissivity correction (Anderson et al., 1997). This is analogous to the use of within-scene temperature scaling in locally calibrated algorithms like METRIC, but in ALEXI the scaling is in time rather than in the space domain.

ALEXI is based on the Two-Source Energy Balance (TSEB) land surface representation of Norman, Kustas, and Humes (1995) with improved parameterizations described in Kustas and Norman (1999). The TSEB treats the radiometric temperature (T_{RAD}) as the average of soil (T_s) and vegetation (T_c) temperature components weighted by fractional vegetation cover (f_c). These component temperatures are used to solve the energy balance for the soil (subscript s), canopy (subscript c) and combined system associated with a mixed pixel:

$$(Rn_s + Rn_c) - G = (H_s + H_c) + (\lambda E_s + \lambda E_c) \tag{1}$$

where Rn is net radiation, G is the soil heat flux, H is sensible heat, and λE is latent heat. T_s and T_c constrain estimates of H_s and H_c, partitioning of net radiation between the soil and canopy layers, as well as G. Canopy transpiration λE_c is estimated using a modified Priestley–Taylor approach with the coefficient indirectly regulated by stress signals conveyed by T_c, and the soil evaporation, λE_s, is computed as a residual to Eq. (1).

To support regional applications, ALEXI couples TSEB with an atmospheric boundary layer (ABL) model to simulate changes in near-surface air temperature (T_a) that are consistent with TSEB modeled surface fluxes (Anderson et al., 1997, 2007). The TSEB is applied at two times during the morning hours, at approximately 1.5 h after local sunrise (t_1) and 1.0 h before local noon (t_2). The ABL component of ALEXI relates the rise in T_a within the mixed layer over the time interval (t_1 to t_2) to the time-integrated influx of H from the surface, thus providing a means for surface energy closure (McNaughton & Spriggs, 1986; Anderson et al., 1997). Anderson et al. (1997) demonstrated that ALEXI is most sensitive to the change in T_{RAD} between t_1 and t_2, and relatively insensitive to absolute bias in T_{RAD}. This approach also eliminates the need for specifying T_a boundary conditions to the sensible heat computations a priori.

For this study, GOES-East and -West Imager instruments provided the 11 μm brightness temperature observations used to determine T_{RAD} at a 4-km spatial resolution (Hain, Crow, Anderson, & Yilmaz,

2014). ALEXI-retrieved latent heat flux (λE_2) at time t_2 (just before local noon) is upscaled to 24-h time-integrated daily ET (ETd, mm d^{-1}) using the ratio of instantaneous to daily insolation:

$$ETd = f_{SUN} * Rs_{24}/\lambda \tag{2}$$

where $f_{SUN} = \lambda E_2 / Rs_2$ is the ratio of latent heat to insolation at time t_2, Rs_{24} (MJ m^{-2} d^{-1}) is the time-integrated daily insolation rate, and λ is the latent heat of vaporization. Cammalleri, Anderson, and Kustas (2014) compared several daily upscaling techniques, including use of reference ET and evaporative fraction, and found the insolation technique to be the least biased and least sensitive to errors in retrieval estimates when tested at an ensemble of flux tower sites within the US, and over multiple seasonal cycles.

Gaps in the daily ET maps, primarily due to cloud cover which prevents LST retrieval using thermal band imagery, were filled using a technique described by Anderson, Kustas, et al. (2012), preserving the ratio of actual-to-reference ET (f_{RET}) during the gap periods. The f_{RET} timeseries are filtered, smoothed and gap-filled at each pixel using a Savitzky–Golay filter in an effort to reduce day-to-day noise while still preserving signals associated with real changes in surface moisture conditions. Daily ET is recovered by multiplying the gap-filled f_{RET} fields by maps of daily reference ET, computed using the Food and Agriculture Organization (FAO) Penman–Monteith formulation for a grass reference site (Allen et al., 1998).

For a detailed description of the ALEXI model, the reader is referred to Anderson et al. (1997, 2007). Additional model inputs are discussed in Section 3.3, below.

2.2. DisALEXI

To map flux distributions at higher spatial resolution than can be supported by geostationary satellite data, an ALEXI flux disaggregation scheme known as DisALEXI can be implemented (Norman et al., 2003; Anderson et al., 2004; Anderson, Kustas, et al., 2012). This disaggregation approach uses higher resolution TIR imagery from sensors like Landsat, MODIS and even airborne sensors (Anderson et al., 2011; Anderson, Kustas, et al., 2012) to spatially disaggregate the coarser-resolution ALEXI flux estimates. The TSEB is run over each ALEXI pixel

area within the modeling domain using high resolution LST imagery acquired at the time of the Landsat/MODIS/aircraft overpass. The air temperature boundary condition (set at a nominal blending height of 50 m) for that ALEXI pixel area is iteratively adjusted until the aggregated 24-h ET, spatially averaged over the ALEXI pixel, matches the ALEXI 24-h ET. The reader is referred to Anderson, Kustas, et al. (2012), Cammalleri et al. (2013) and Cammalleri, Anderson, Gao, et al. (2014) for further description. In this way, flux conservation is enforced at the scale of the ALEXI pixel (4 km in this case) between multi-scale ET assessments.

Within the data fusion package, ETd maps are created at 30-m spatial resolution on predominantly clear Landsat overpass dates using Landsat thermal imagery sharpened to 30-m as described in Section 3.3.1.1. In addition, ETd maps were created at 1 km resolution for each day during the modeling period using the MODIS swath LST product. The MODIS ETd maps were gapfilled in a manner analogous to the ALEXI ET time series, by smoothly preserving f_{RET} between sampling dates. These maps were then resampled onto the Landsat 30 m (UTM) grid using nearest neighbor interpolation for ingestion into STARFM.

2.3. STARFM

The Spatial and Temporal Adaptive Reflectance Fusion Model (STARFM) (Gao et al., 2006) was used to fuse the periodic 30-m resolution Landsat ET maps with the daily 1-km MODIS maps to form a daily 30-m ET product. Again, consistency between Landsat and MODIS ET is achieved by using the ALEXI ET as a common normalization field in DisALEXI. STARFM develops spatially distributed weighting factors describing the spectral and spatial relationship between an existing Landsat/MODIS image pair that is then used to govern the disaggregation of MODIS images on days when Landsat data are not available (the prediction date). The optimal training pair for a given prediction date is selected by searching all possible pairs (where there are Landsat and MODIS retrievals on the same day) and determining which MODIS scene among these pairs is best correlated with the MODIS image on the prediction date. The derived weighting function is then applied to the MODIS image on the prediction date to disaggregate the image to Landsat scale. In this application, a single training pair was used for each prediction date, although STARFM also allows use of two training pairs from bracketing dates. The reader is referred to Gao et al. (2006) for more details on the STARFM algorithm, and Cammalleri et al. (2013) and Cammalleri, Anderson, Gao, et al. (2014) for a schematic describing applications of STARFM to ET data fusion.

Instantaneous and daily surface energy balance components on Landsat dates, as well as fused daily ET over the full study period, were extracted from the 30-m UTM grids at the site of the two towers using a flux footprint model based on approximations from Hsieh, Katul, and Chi (2000), with fetch extending upwind of the tower and horizontal dispersion related to standard deviation in wind direction as described in Li, Kustas, Anderson, Prueger, and Scott (2008).

3. Experimental site and datasets

3.1. Study area

Wine grape production is expanding in the Central Valley region of California, an area with characteristic warm days and cool nights and an evaporative demand ranging from 889 to 1270 mm of water during the growing season (Williams, 2001). As part of the USDA-ARS Grape Remote sensing Atmospheric Profiling and Evapotranspiration eXperiment (GRAPEX), two Pinot noir vineyards, located at the border of Sacramento and San Joaquin counties (Fig. 2), were instrumented in 2013 with flux towers and in-field ground measurements of soil moisture and temperature. The larger, northern field (Site 1; 34.4 ha) is more mature (7–8 years old) while the vines in the southern field (Site 2; 21 ha) are 4–5 years old. The height of the vines ranges between 2 and 2.5 m,

with row spacing approximately 3.35 m and average vine spacing along the row of 1.52 m. Both fields have east–west row orientation. Because winds are typically from the west in this area, the towers were located on the eastern edge of the fields such that the dominant fetch for both towers typically lies within the target field boundaries.

Soil moisture is carefully controlled throughout the growing season to regulate vine water availability at different phenological stages. A grass cover crop between vine rows germinates in the late winter/early spring and is used to deplete soil moisture that accumulates from winter rains. This inter-row grass canopy remains green until late May/early June when temperatures rise and the dry season commences. In some years, the cover crop may be mowed prior to senescence to further control soil moisture evolution in a given field (see photograph of Site 2 in Fig. 2 from the 2014 growing season). Drip irrigation typically commences sometime later in June and is continued until harvest if necessary. Decisions to begin irrigation in a field for a season are triggered by various factors, including visual assessment of canopy water stress, spot measurements of leaf water potential with pressure chambers, soil moisture and upcoming weather conditions. Harvest for Pinot noir in the Central Valley typically occurs in early September. In 2013, the average yield in the northern field was 25.76 t ha^{-1} (metric tons per hectare), while in the southern field it was 16.93 t ha^{-1}.

The area immediately surrounding the study fields is mainly vineyards of varying cultivars and ages (Fig. 3). New vineyards are being planted at rapid rates in this area and throughout the county to meet the growing demand for California wines. Other cultivated areas in the vicinity of the Lodi vineyards include some fields of hay and alfalfa, as well as a few nut tree orchards. Surrounding the cultivated area along the streambed are large expanses of unirrigated pasture and grassland, which senesce rapidly in the summer resulting in low ET and high LST (red areas in Fig. 2).

3.2. Micrometeorological and biological field measurements

GRAPEX measurements include ground, airborne, and satellite remote sensing, surface energy balance, turbulence and mean profile measurements of wind, temperature and water vapor focusing on above, below and between vine canopies, surface and sub-surface soil moisture, along with ground-based biophysical measurements of leaf area index (LAI) and leaf-level conductance, transpiration and photosynthesis. Micrometeorological measurements commenced on day of year (DOY) 97 (April 7) in 2013, and continued through 2014 and into 2015. Several intensive observation periods (IOPs) were conducted in 2013–2015 to collect biophysical measurements of the vine canopy during different phenological stages, and high resolution airborne imagery coincident with Landsat 8 overpass times to provide validation of satellite derived variables. This study focuses on data collected during the 2013 growing season (DOY 97-300).

The two vineyards were instrumented with identical tower-based sensor packages. Focusing on the micrometeorological and surface flux measurements associated with the eddy covariance (EC) technique, these sensors include a sonic anemometer (CSAT3, Campbell Scientific, Logan, Utah), which measures the orthogonal wind velocity components, co-located with an open-path gas analyzer (EC-150, Campbell Scientific) measuring concentrations of water vapor and carbon dioxide. Both instruments were mounted 5 m above ground level (agl) facing due west and operated at a sampling frequency of 20 Hz. (The mention of trade names of commercial products in this article is solely for the purpose of providing specific information and does not imply recommendation or endorsement by the US Department of Agriculture.)

Additional instruments above-ground include a four-component net radiometer (CNR-1, Kipp and Zonen, Delft, Netherlands) mounted at 6 m agl, upward and downward facing quantum sensors (LI-190, Li-Cor, Lincoln, Nebraska) mounted at 6 m agl to measure incident and reflected photosynthetically active radiation, a combined humidity and
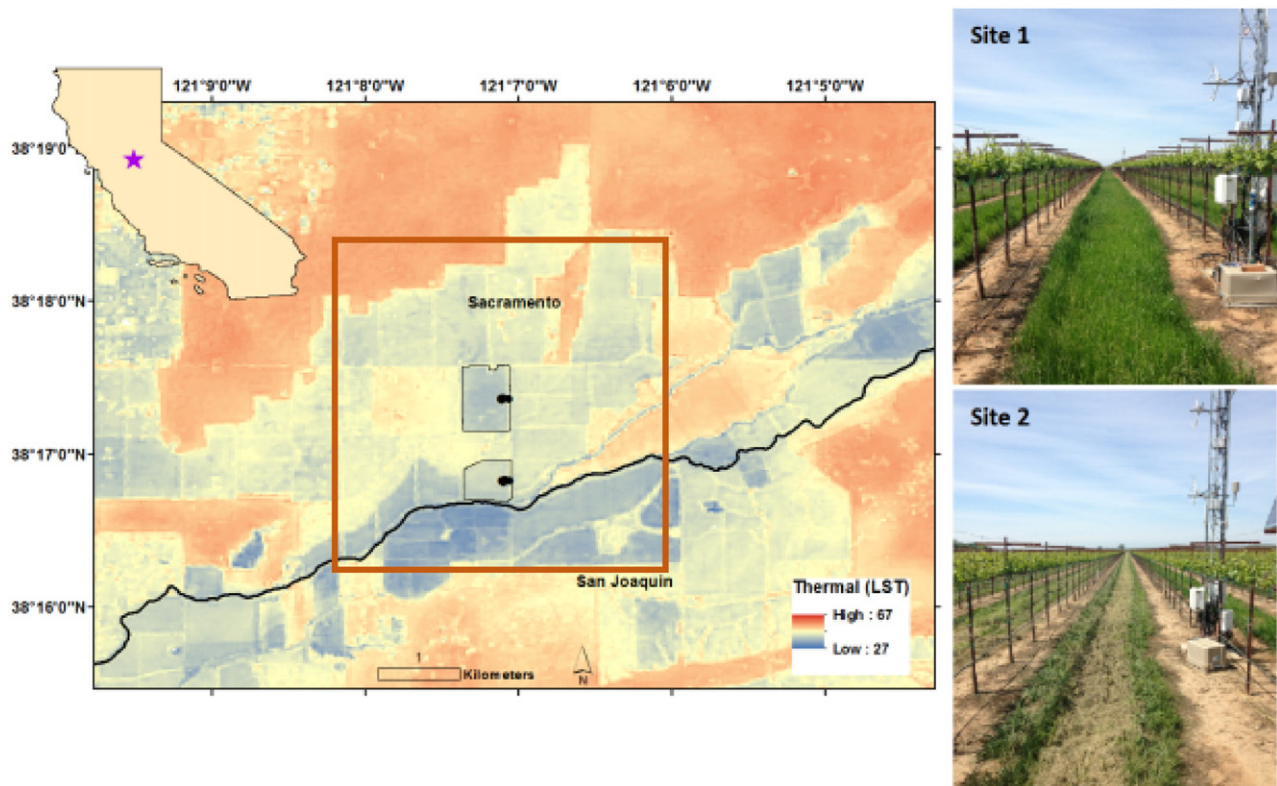
Fig. 2. Landsat 8-derived land surface temperature (°C), sharpened to 30 m spatial resolution, over the study area in central California, Sacramento County at the border (black line) to San Joaquin County on July 14th, 2013 at 18:41 UTC. Outlined fields highlight Site 1 to the north (7–8 year old Pinot noir vines) and Site 2 to the south (4–5 year old Pinot noir vines). Black dots denote flux tower locations and soil moisture locations near the towers. Site photos to the right show the maturity of the vines and condition of cover crop on April 8, 2014 (the year after the study period examined here), as well as the flux tower instrumentation. The orange box indicates the nominal 4 km ALEXI pixel size.

temperature sensor (HMP45C, Vaisala, Helsinki, Finland) mounted at 5 m, a pair of thermal infrared thermometers (SI-111, Campbell Scientific) mounted at 2.5 m to measure surface and canopy temperature, and a tipping bucket rain gauge (TE525, Texas Electronics, Dallas, Texas). Subsurface sensors include a cross-row transect of five soil heat flux plates (HFT-3, Radiation Energy Balance Systems, Bellevue, Washington) buried at a depth of 8 cm. Each heat flux plate was paired with two thermocouples buried at 2 and 5 cm depths and a soil moisture probe (HydraProbe, Stevens Water Monitoring Systems, Portland, OR) buried at a depth of 5 cm. The soil surface heat flux (G) measurement includes the soil heat flux across the heat flow transducer (G_T) and heat storage in the soil layer above the transducers (S), such that $G = G_T + S$ (see e.g., Brutsaert, 1982). Soil moisture in the storage layer was estimated from the HydraProbe soil moisture sensors near each soil heat flux sensor package. There were also three soil moisture profile systems installed within 100 m of each tower with sensors located at 30, 60 and 90 cm depths. Volumetric soil water and temperature were recorded hourly at these depths.

The eddy covariance data were processed with temperature and vapor pressure measurements used to correct for oxygen and density effects on the evaporative and carbon fluxes (Webb–Pearman–Leuning—WPL correction; Webb, Pearman, & Leuning, 1980). Further processing included applying a 2-D coordinate rotation (CR) forcing $v = w = 0$ (Kaimal & Finnigan, 1994) and corrections for sensor displacement (SD) and frequency response (FR) attenuation (Massman & Lee, 2002). The CR and FR corrections were found to have a relatively small effect on the fluxes compared to the WPL. In addition to the turbulent fluxes, mean wind speed and wind direction were computed from the CSAT3 measurements. Typical closure ratios $(H + \lambda E)/(Rn - G)$ for daytime conditions where $Rn > 0$ were on the order of 0.91 for Site 1 and 0.80 for Site 2. For comparison with modeled energy balance estimates,

the observed fluxes were corrected for closure errors by assigning the residual to the latent heat flux (Prueger et al., 2005).

In addition to micrometeorological data, episodic biophysical measurements were also collected during GRAPEX to monitor LAI development in the cover crop and vines. The LAI measurements were made using a Li-Cor LAI-2000 instrument along several transects collecting 4 samples (under the vine, a quarter of the distance from the vine row, in the center of the inter-row, and ¾ of the distance from the vine row) to obtain an estimate of the effective LAI of the vine/inter-row system. Measurements were made with and without including the inter-row cover crop, which had a very minor impact on the LAI measurements for the field IOPs in June and August. Vines grow in the early spring and rapidly expand in leaf area mid to late May, and the observed LAI increased throughout the season until harvest in early September.

In addition, yield maps for the 2013 harvest in both fields were provided by E & J Gallo Winery, generated following the protocol of Bramley and Williams (2001). Advanced Technology Viticulture (ATV, Joslin, Australia) yield monitor systems were installed on three self-propelled, over-the-row, trunk-shaking mechanical GH9000 AIM harvesters (Agricultural Industrial Manufacturing, Lodi, CA, USA). Yield monitors consist of a combined dGPS receiver and antenna as well as a specialized grape weighing and data recording system consisting of a load cell weight bridge, belt speed sensor and data logger. Harvest data were transferred into a clean-up script written in R Studio software (RStudio Inc., Boston, MA, USA) to convert mass flow units into tons per hectare, eliminate outliers, and normalize harvesters. Yield data points more than three standard deviations from the mean were removed to reduce scatter which usually results in less than 5% of total yield point removal. After clean-up, the data were kriged to 3 × 3 m resolution grids.
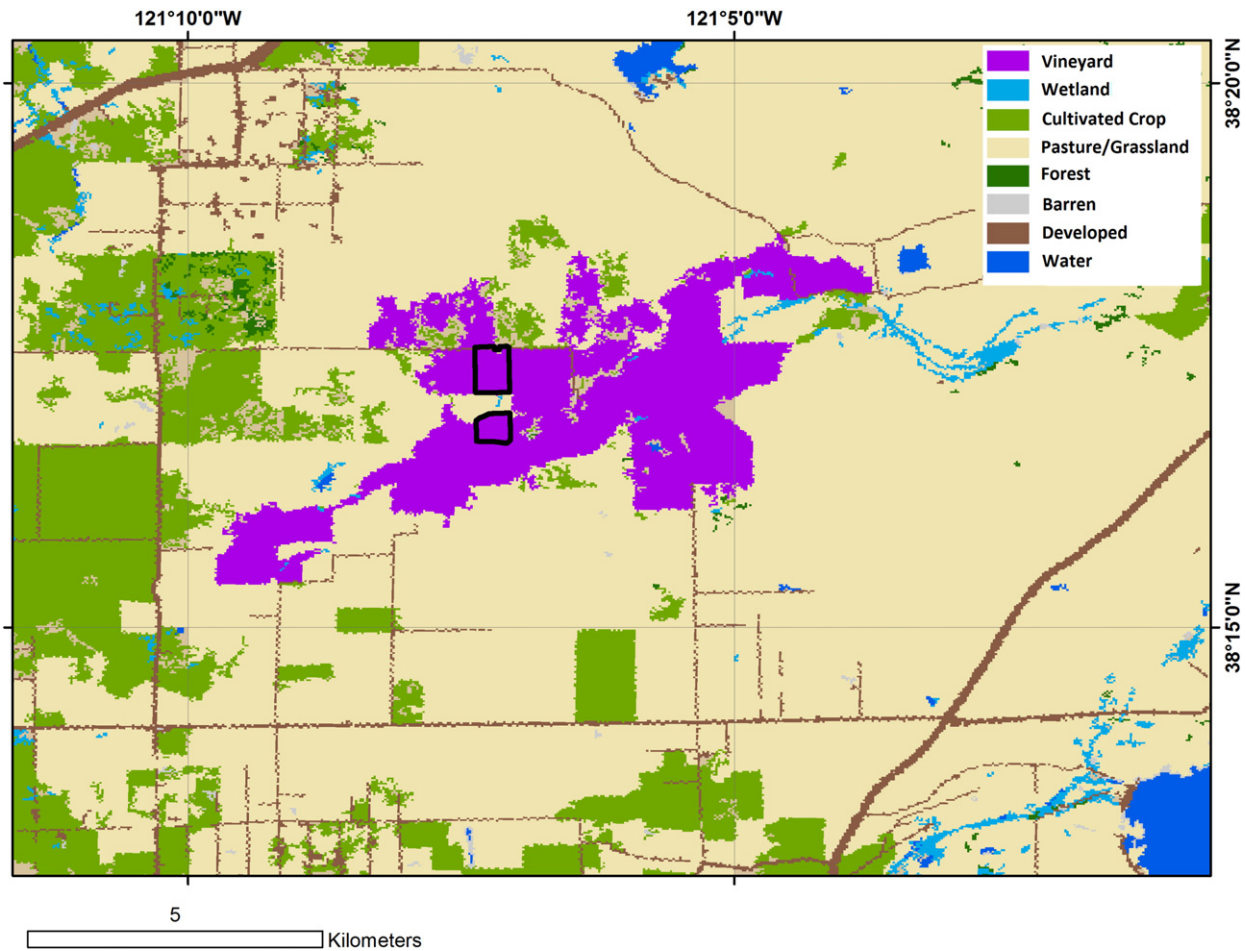
Fig. 3. Landcover classification map used in DisALEXI processing. National Land Cover Dataset (NLCD) data were modified to include a vineyard classification for the study area.

3.3. Model inputs

3.3.1. Remote sensing data

3.3.1.1. DisALEXI-Landsat. Landsat 8 (L8) data between DOY 90 and 300 of 2013 were collected over the study area (lying in the overlap between path 43/row 33 and path 44/row 33) and a total of 22 scenes were processed (see Table 1). Data from the L8 TIRS band 10 were atmospherically corrected using MODTRAN (Berk, Bernstein, & Robertson, 1989) following procedures described by Li et al., 2004. Measurements of the atmospheric profile from radiosonde observations, ozone and visibility estimates were input to MODTRAN to obtain path radiance and down-welling sky radiance and transmittance, and used to produce surface brightness temperature. The assumed emissivity fields used to convert to surface radiometric temperature (T_{RAD}, or LST) were based on the methods of French et al. (2005) using estimates of fraction vegetation cover (Anderson et al., 2007). The resulting 100-m LST images (native TIRS resolution) were spatially sharpened to the 30-m resolution of the shortwave L8 bands using a Data Mining Sharpener (DMS) technique based on regression tree analysis (Gao, Kustas, & Anderson, 2012). This significantly enhances the sharpness of field boundaries, while still conserving energy at the native 100-m scale of the TIRS sensor.

Shortwave reflectance band data from L8 were calibrated and atmospherically corrected using a modified version of the Landsat Ecosystem Disturbance Adaptive Processing System (LEDAPS; Masek et al., 2006). Broadband visible and near-infrared albedo were extracted from the six reflectance bands output from LEDAPS according to Liang, 2000. In addition, 30 m maps of leaf area index (LAI) were derived using a

regression tree analysis trained with MODIS 1 km LAI data to maintain consistency in LAI between Landsat and MODIS processing (see Gao, Anderson, Kustas, & Wang, 2012; Cammalleri et al., 2013). All model

Table 1
List of 22 Landsat 8 scenes used in this study, DOY and time of acquisition, path and row, and the transmittance and upwelling path radiance (W m^{-2} µm^{-1} sr^{-1}) output from MODTRAN used to atmospherically correct the thermal band.

Year	DOY	HHMM (UTC)	Path	Row	Transmittance	Upwelling path radiance
2013	106	18:47	44	33	0.923	0.485
2013	115	18:41	43	33	0.803	1.567
2013	131	18:41	43	33	0.875	0.913
2013	154	18:47	44	33	0.746	1.995
2013	163	18:41	43	33	0.731	2.215
2013	170	18:47	44	33	0.789	1.601
2013	179	18:41	43	33	0.808	1.482
2013	186	18:47	44	33	0.886	0.965
2013	195	18:41	43	33	0.787	1.672
2013	202	18:47	44	33	0.823	1.218
2013	211	18:41	43	33	0.871	0.952
2013	218	18:47	44	33	0.825	1.257
2013	227	18:41	43	33	0.868	1.048
2013	234	18:47	44	33	0.852	1.177
2013	243	18:41	43	33	0.777	1.949
2013	250	18:47	44	33	0.837	1.282
2013	259	18:41	43	33	0.785	1.693
2013	266	18:47	44	33	0.733	2.236
2013	275	18:41	43	33	0.695	2.443
2013	282	18:47	44	33	0.785	1.728
2013	291	18:41	43	33	0.865	1.034
2013	298	18:47	44	33	0.892	0.866

input fields were subset to a study area mask for use within DisALEXI. The CFmask cloud mask layer (Zhu, Wang, & Woodcock, 2015), recently included in the Landsat surface reflectance climate data record distributed by the EROS Data Center, was applied to screen out cloud impacted areas of the domain.

3.3.1.2. DisALEXI-MODIS. Daily MODIS LAI maps were generated from the 4-day composite product (MCD15A3, Collection 5; Myneni, 2014). These 4-day maps were smoothed and gapfilled to daily timesteps following the procedure described by Gao et al. (2008), which uses the TIMESAT algorithm for analyzing satellite time-series data for seasonality and other temporally dynamic vegetation properties (Jönsson & Eklundh, 2004). The smoothing procedure gives higher weight to clear-sky and high quality MODIS LAI retrievals, as identified in the product quality control layers. Daily MODIS NDVI maps were generated from 16 day composites (MOD13A2, Collection 5; Huete, Justice, & Leeuwen, 2014). Input MODIS albedo maps were generated from the Solar Zenith Angle (SZN)-extended MODIS/Terra + Aqua 30 arc sec Global Gap-Filled Snow-Free Bidirectional Reflectance Distribution Function (BRDF) (MODIS BRDF/Albedo CMG Gap-Filled Snow-Free Product MCD43GF V005) parameters product available by request from University of Massachusetts Boston (Dr. Crystal Schaaf). Daily albedo was calculated using solar zenith angle and total albedo calculated as the weighted average of white (25%) and black sky (75%) albedo assuming a nominal partitioning of diffuse and direct beam radiation under clear-sky conditions. Daily LAI, NDVI, and albedo were estimated using a spline interpolation. MODIS LST and view angle maps were generated from Terra instantaneous swath 1 km data (MOD11_L2, Collection 5; Wan, 2014) using the MODIS Conversion Toolkit (version 2.0) and geolocation fields (MOD03) to obtain correct georegistration. LST was sharpened using DMS to reduce the bowtie effect due to off-nadir pixel smearing. In this case, DMS was run using the 1 km MODIS NDVI, effectively reproducing the sharpening procedure (Kustas, Norman, Anderson, & French, 2003) used in prior implementations of DisALEXI (Cammalleri Anderson, Gao, et al., 2013, 2014).

3.3.1.3. ALEXI-GOES. ALEXI was executed on daily timesteps over a domain covering the contiguous United States at a spatial resolution of 4 km. LST inputs were computed from 11 μm brightness temperature observations from the GOES-EAST (at 75°W) and GOES-WEST (at 105°W) Imager instruments at a spatial resolution of 4-km (nadir). The raw brightness temperature observations were atmospherically corrected using atmospheric profiles of temperature and mixing ratio following the single channel algorithm of Price (1983). Atmospheric profiles of temperature and mixing ratio used in the atmospheric correction were computed from the NCEP Regional Reanalysis (NARR) dataset (Mesinger et al., 2006). Cloud-free pixels are determined by using the bi-spectral composite threshold technique which applies a series of threshold tests using GOES 3.7 and 11.0 μm brightness temperature measurements (Jedlovec, Haines, & LaFontaine, 2008). Vegetation cover fraction was obtained from the 4-day MODIS leaf area index product, and albedo information from 16-day MODIS albedo composites (MOD43C; Moody, King, Platnick, Schaaf, & Gao, 2005. Hourly incoming shortwave and longwave radiation were provided from the National Land Data Assimilation System-2 (NLDAS-2) meteorological forcing dataset at a 0.125° spatial resolution (Cosgrove et al., 2003).

3.3.1.4. High resolution aircraft imagery. During the GRAPEX13 experiment, high resolution aircraft thermal imagery were obtained periodically from a system operated by Utah State University and used in prior USDA field experiments (Anderson et al., 2004, 2005, Chavez, Neale, Hipps, Prueger, & Kustas, 2005; Neale et al., 2012). These images were used as input to DisALEXI to confirm structure apparent in the Landsat-resolution ET maps. The system consists of three Kodak Megaplus1 4.2i digital cameras with interference filters forming spectral bands in the green (0.545–0.555 μm), red (0.665–0.675 μm) and near infrared (NIR) (0.790–0.810 μm) wavelengths. The TIR images were acquired with an Inframetrics 760 Scanner in the 8–12 μm range. Details of image acquisition and processing can be found in Neale et al. (2012). Visible and thermal band imagery used in this study were collected on June 12, 2013 (DOY 163) at ~13:15 PST, approximately 2.5 h after the L8 overpass of the GRAPEX site. The original resolution was 0.05 m for the visible bands (NIR (0.8 μm), Red (0.655 μm), and Green (0.562 μm)) and 0.38 m for the thermal band. All bands were aggregated through averaging to 5 m resolution. A simple linear regression between Landsat 8 and the aircraft thermal imagery ($R^2 = 0.76$) was used to adjust the airborne thermal data for the time difference in the acquisition before running DisALEXI. Aircraft red and NIR imagery from the prior day (DOY 162) were used due to issues with the shortwave sensors on DOY 163. An exponential function was fit between Landsat 8 LAI and aircraft NDVI, with a R^2 value of 0.98. This fitted function was used to provide 5-m resolution LAI inputs to DisALEXI.

3.3.2. Regional meteorological inputs

ALEXI/DisALEXI also require several meteorological inputs for execution, including time-series of hourly solar radiation and wind speed for each modeling date, along with air temperature and vapor pressure fields used for computing reference ET used in the temporal gap-filling of ALEXI and DisALEXI-MODIS fields. In addition, ALEXI requires pre-dawn profiles of atmospheric potential temperature for the ABL closure routine. In this study hourly insolation, temperature, wind and pressure fields were obtained from the NARR dataset (Mesinger et al., 2006). These fields were mapped to the 4 km ALEXI grid and converted to each sensor's projection at both daily and overpass times for ingestion into DisALEXI.

3.3.3. LANDCOVER

Landcover class is used to specify surface roughness parameters and vegetation optical properties used in ALEXI/DisALEXI (Anderson et al., 2007). The ALEXI model uses the University of Maryland (UMD) global land cover dataset at 1-km resolution, based on observations from the Advanced Very High Resolution Radiometer (AVHRR; Hansen, DeFries, Townshend, & Sohlberg, 2000). For the higher resolution MODIS and Landsat disaggregation experiments, landcover classification (Fig. 3) was determined from the 30 m National Land Cover Dataset (NLCD; Fry et al., 2011). For MODIS, the NLCD map was upscaled to 1 km using the highest percentage class within each MODIS pixel. In addition, the landcover classification was modified in ArcGIS to include a vineyard classification as a rough approximation (Fig. 3). In DisALEXI, a nominal vegetation height of 2.3 m was used to compute roughness parameters for pixels with vineyard classification.

4. Results and discussion

4.1. Model evaluation

Flux estimates from DisALEXI-Landsat on Landsat overpass dates, averaged over the tower footprint using methods described by Li et al. (2008), are compared to EC observations in Fig. 4, both for instantaneous (Landsat overpass time) retrievals and upscaled 24-h estimates. At both the north site (Site 1) and south site (Site 2), simulated instantaneous and 24-h fluxes (net radiation, latent heat, sensible heat, soil flux, solar radiation) on Landsat observation dates fall generally along the one-to-one line against in-field measurements. Quantitative measures of all flux comparisons are shown in Table 2. Modeled insolation and net radiation agree well with local measurements, indicating the NARR radiative forcing inputs and assumed bulk albedo are reasonable at these two sites. Landsat-derived 24-h ET fluxes have low root mean square errors (RMSE) of 0.63 to 0.67 mm/d for both sites, while the percent error in ET estimates on Landsat dates (expressed as mean absolute difference [MAD] divided by the mean observed flux, following
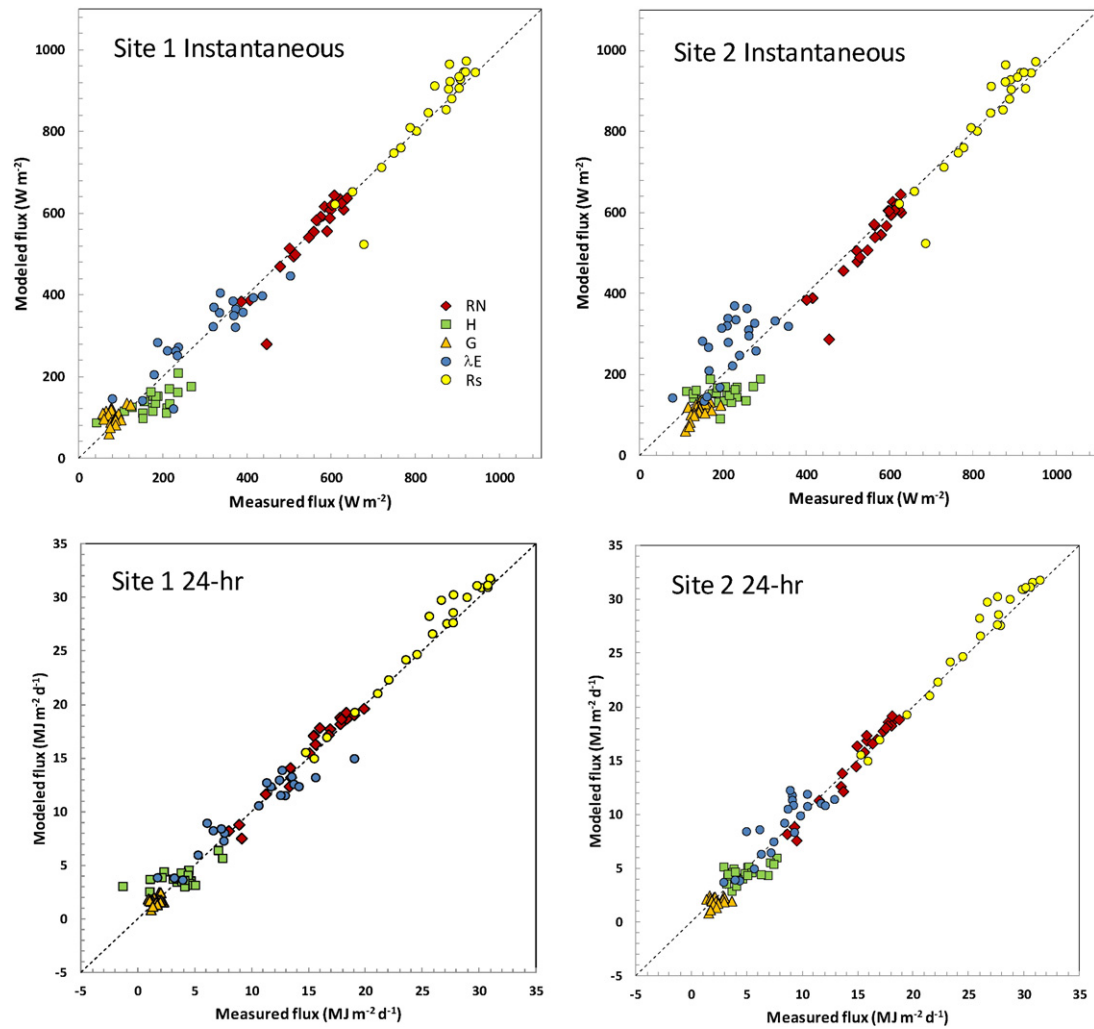
Fig. 4. (Top panels) Scatterplots comparing observed fluxes and estimates obtained with DisALEXI-Landsat on Landsat overpass dates for instantaneous fluxes (*Rs* — solar radiation, *Rn* — net radiation, *λE* — latent heat, *H* — sensible heat, *G* — soil flux) for the two flux tower sites. (Bottom panels) Scatterplots comparing observed and Landsat-retrieved 24-h fluxes for two flux tower sites in the vineyards.

Table 2
Statistical measures of model performance at Sites 1 and 2 at instantaneous and 24-h (d) timesteps for Landsat overpass dates, and for STARFM daily and weekly output between DOY 100-300.

Site	Variable Unit	Rn W m^{-2}	H W m^{-2}	G W m^{-2}	LE W m^{-2}	Rnd MJ m^{-2} d^{-1}	Hd MJ m^{-2} d^{-1}	Gd MJ m^{-2} d^{-1}	LEd MJ m^{-2} d^{-1}	ETd mm d^{-1}	ET(Fusion) mm d^{-1}	ET(Fusion) mm wk^{-1}
1	n	22	22	22	22	22	22	22	22	22	199	28
1	Mean P	549	135	103	311	15.72	3.85	1.71	10.16	4.15	4.18	29.53
1	Mean O	553	173	79	297	15.25	3.65	1.49	9.95	4.06	3.97	28.14
1	MBE	−4	−37	25	13	0.47	0.20	0.22	0.21	0.09	0.21	1.39
1	RMSE	39	50	32	47	0.91	1.51	0.50	1.54	0.63	0.92	4.93
1	MAD	22	41	26	38	0.74	1.09	0.42	1.18	0.48	0.71	4.04
1	% error	3.9	24.0	33.2	12.7	4.8	29.8	28.4	11.9	11.9	18.8	14.4
1	r^2	0.86	0.53	0.09	0.55	0.97	0.34	0.06	0.83	0.83	0.67	0.76
2	n	22	22	22	22	22	22	22	22	22	199	28
2	Mean P	537	153	112	272	15.30	4.54	1.95	8.82	3.60	3.68	25.96
2	Mean O	556	195	143	219	15.11	4.84	2.17	8.11	3.31	3.24	22.89
2	MBE	−19	−42	−31	54	0.19	−0.30	−0.22	0.71	0.29	0.44	3.07
2	RMSE	42	63	35	79	0.87	1.22	0.65	1.63	0.67	0.96	5.76
2	MAD	26	55	31	64	0.70	1.01	0.55	1.26	0.51	0.75	4.50
2	% error	4.7	28.0	22.0	29.2	4.6	20.8	25.2	15.5	15.5	23.2	19.6
2	r^2	0.87	0.03	0.40	0.40	0.97	0.31	0.04	0.73	0.73	0.46	0.49

a. ET — Evapotranspiration; *Rn* — net radiation; *H* — sensible heat; *G* — soil flux; *λE* — latent heat; Fusion columns summarize daily and weekly ET output over the full course of the experiment, d — 24-h fluxes on Landsat dates; the rest are fluxes at the time of Landsat overpass.
b. n — number of data points; mean P — mean predicted/modeled; mean O — mean observed; MBE — mean bias error (mean P − mean O); RMSE — root mean square error; MAD — mean absolute difference (abs($\overline{P-O}$)); % error — percent error is the mean absolute difference divided by the mean observed flux; r^2 — coefficient of determination in regression of P on O.

recommendations by Willmott, 1982; Willmott & Matsuura, 2005) is 12% for Site 1 and 16% for Site 2 — consistent with results obtained in earlier studies using DisALEXI (Anderson, Kustas, et al., 2012; Cammalleri et al., 2013; Cammalleri, Anderson, Gao, et., 2014).

Statistics are also provided in Table 2 for daily and weekly 30-m ET estimates from the STARFM fusion algorithm ("Fusion" ET), including both Landsat overpass dates and dates between overpasses. The percent errors from the fused daily time series are somewhat larger than for the Landsat dates alone, with values of 19% for Site 1 and 23% for Site 2 and with RMSE of 0.92 and 0.96 mm/d, respectively. An increase in error is to be expected, since the majority of the days in this timeseries are recovered by fusion rather than direct retrieval from Landsat imagery. At the weekly timestep, relevant to irrigation management, percent errors reduce to 14 and 20% due to time-averaging of random errors. The difference in apparent model performance between Sites 1 and 2 is due primarily to an early season bias at Site 2, which is discussed in detail in Section 4.2.

The average modeled and measured ET over the course of the experiment is between 3 and 4 mm d^{-1}, with higher rates of water consumption at Site 1 (more mature) than at the younger Site 2. The average ET values reported here are consistent with other studies of water use in vineyards; for example, Teixeira et al. (2007) reported average ET of 3.3 mm d^{-1} in irrigated vineyards in the São Francisco river basin, Brazil, a semi-arid region with average rainfall of 570 mm per year and monthly air temperature averages of 24–30 °C. The correspondence to in-field measurements supports the applicability of this remote sensing approach to monitoring energy flux and evapotranspiration dynamics in vineyards.

4.2. Temporal patterns in evapotranspiration (ET)

Timeseries of observed and modeled daily ET for the 2013 growing season at Sites 1 and 2 are shown in Fig. 5. On average over this period, the observed ET at Site 1 was 80% of reference ET — matching the target believed to maximize berry size (Williams, 2001). Observed seasonal cumulative ET at Site 2 was about 82% of the seasonal ET value for Site 1, but with similar reference ET conditions, resulting in an average actual-to-reference ET ratio of 65% for this tower site.

The utility of disaggregation as a validation tool is clearly apparent. In general, agreement between model and tower measurements significantly improves in moving from the ALEXI-GOES scale (4-km pixels) to Landsat scale (30 m) — particularly at Site 1. The model estimates at the various scales tend to converge at Site 2 after DOY 210, indicating this tower site is more representative of the local landscape. The role that the MODIS ET plays in guiding the temporal interpolation of 30 m fluxes between Landsat overpasses is evident in the STARFM timeseries. For comparison with STARFM, results are also shown from a simple Landsat-only interpolation scheme conserving the ratio of actual-to-reference ET through linear interpolation between Landsat overpasses. Cammalleri et al. (2013) found significant improvement in daily ET retrieved using STARFM over the Landsat-only interpolation in an implementation over rainfed soybean fields in central Iowa during SMEX02.
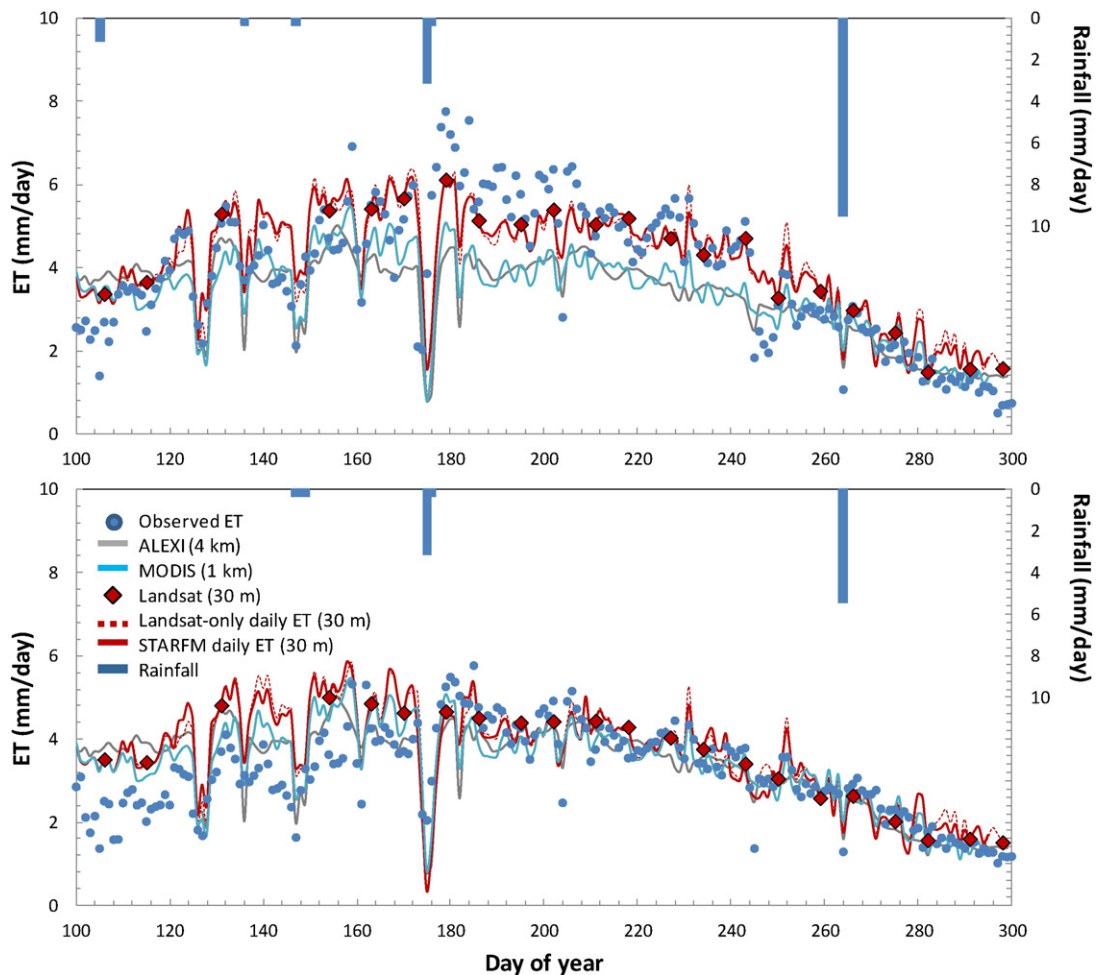

Fig. 5. Time series of observed daily ET (blue dots), ET retrievals from ALEXI (gray line), DisALEXI-MODIS (aqua line) and DisALEXI-Landsat (red diamonds), along with 30 m daily ET estimates from STARFM (solid red line) and Landsat-only interpolation (dotted red line) for Site 1 (top panel) and Site 2 (bottom panel). Rainfall events are shown as blue bars.
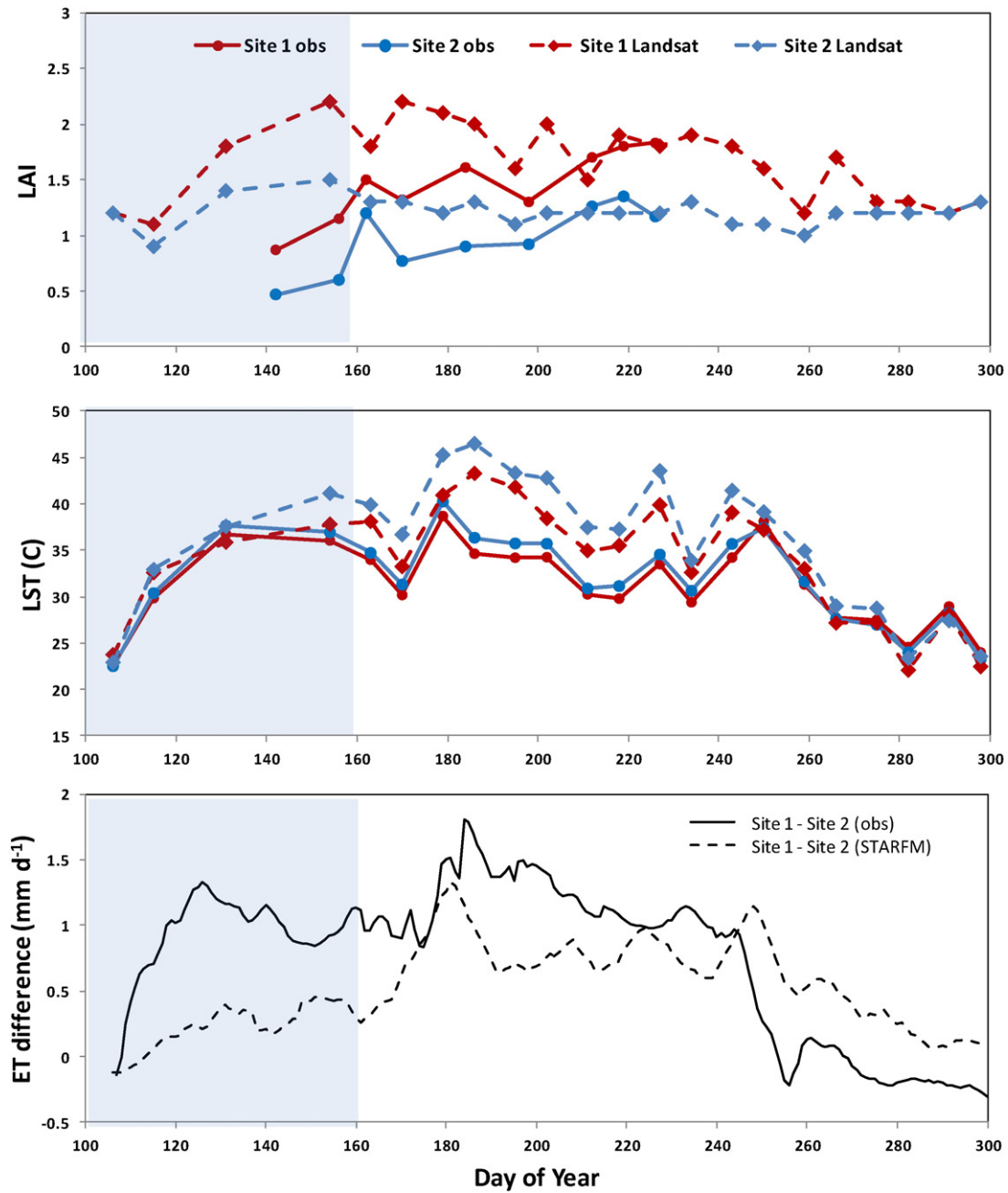
Fig. 6. Comparison of Landsat-retrieved and measured leaf area index (LAI, top panel) and land surface temperature (LST, middle panel) at the time of overpass (~1840 UTC) for each Landsat overpass date at Sites 1 and 2. Bottom panel shows difference in ET between Sites 1 and 2 as inferred from EC observations and the STARFM retrievals, smoothed with a 10-day moving average. The period prior to DOY 160 when the early season model bias at Site 2 is significant has been highlighted.

STARFM was better able to capture ET response to a rainfall event that occurred between Landsat overpasses. In the current study, however, the STARFM and Landsat-only interpolation techniques show similar performance (Fig. 5). This is due to the greatly improved temporal sampling available with Landsat 8 at this California site, given its location within the overlap between adjacent WRS paths and the low cloud cover during the growing season.

At Site 1, ET estimates from the direct Landsat retrievals and the fused daily timeseries largely follow the observed values especially in early and late season. The observed ET is underestimated during the middle part of the season between approximately DOY 180 and 210. This departure is preceded by a large precipitation event on DOY 175. A comparable underestimation in ET is observed during this time period when the TSEB is applied directly to LST, LAI and meteorological data

collected in the field. This may indicate an enhanced localized response to the precipitation event that is not completely captured by the thermal signal, as explored further in Section 4.2.

A similar enhancement in EC measurements of latent heat flux was not observed in Site 2 following this rainfall event, and the fused ET timeseries for Site 2 agrees well with observations during this time period and for the remainder of the experiment season. This is further evidence that the ET enhancement at Site 1 was a very localized surface phenomenon, and not driven by prevailing meteorological conditions. However, water consumption is overestimated at Site 2 in the early season prior to DOY 175. A small wet bias is also evident in the very early season at Site 1, before DOY 106.

There are several possible sources for the early season wet bias in the DisALEXI-Landsat and fused daily ET estimates. It may reflect biases in
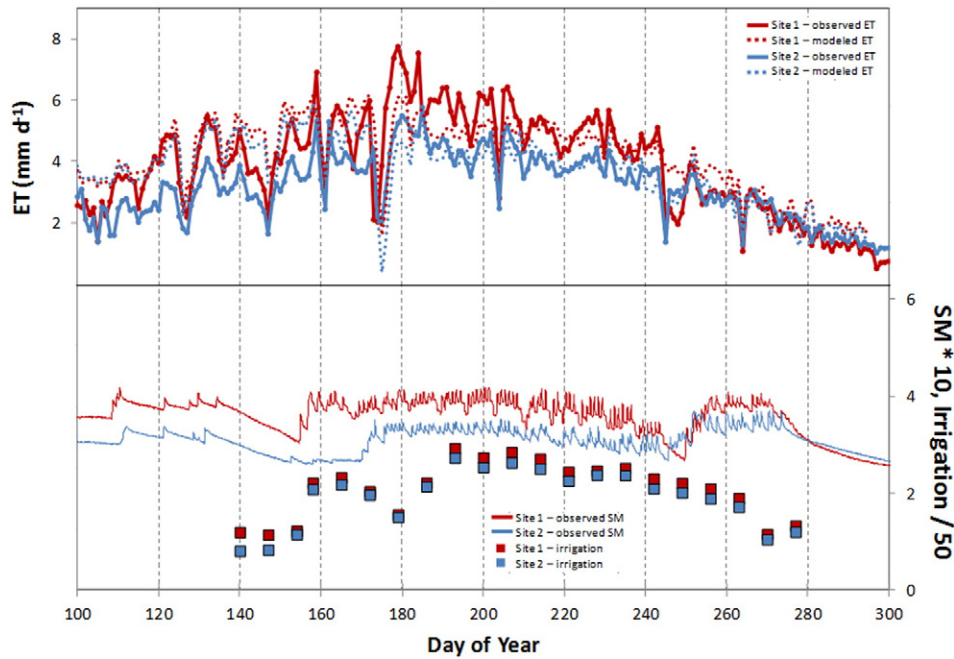
Fig. 7. Time series of observed (solid lines) and fusion modeled (dotted lines) ET for Sites 1 (red) and 2 (blue) are shown in top panel. Average soil moisture (SM; volumetric water content * 10) shown as solid lines in bottom panel is plotted with values on the right axis, as well as approximate weekly irrigation rates shown with squares (liters per vine/50).

the coarse-scale early springtime ALEXI daily ET estimates over this region, which form the basis for the spatial disaggregation accomplished through DisALEXI. To date, studies evaluating ALEXI fluxes through disaggregation have been principally focused on the mid-continent growing season, starting between DOY 130 and 150. There is evidence to suggest that the time window for LST rise signal used in ALEXI during the winter/early spring may need adjustment to compensate for shorter daylength. These adjustments will be evaluated in follow-on studies, looking at continuous model time behavior between the GRAPEX 2013, 2014 and 2015 campaigns. However, given the fact that the early season is reasonably well-modeled at Site 1, lying within the same ALEXI pixel, ALEXI biases may not be the primary issue in this case.

The exacerbated early season bias at Site 2 prior to DOY 160 may also relate to errors in the Landsat retrievals of LAI and LST — the two primary DisALEXI inputs that govern disaggregation of the 4-km ALEXI flux to the subpixel level. Unless the Landsat inputs are significantly different between the two fields, the disaggregation strategy will apportion similar disaggregated fluxes to the two fields. Indeed the difference in STARFM ET between sites appears to be well correlated in time with differences in Landsat LAI and LST retrievals, with relatively small differences observed before DOY 160 (Fig. 5). While there were no LAI observations during the early period, the Landsat-derived LAI appears to overestimate field values until midseason. However, manual adjustment of Landsat LAI inputs to DisALEXI for vineyard pixels toward values observed in Sites 1 and 2 did not appreciably impact the modeled ET. The timeseries in Landsat LST departures between sites appears to follow observations well (Fig. 6). Note that the absolute offset in Landsat LST with respect to observations is not as important as in-scene variability due to the flux normalization step with respect to the 4-km ALEXI-based ET estimates.
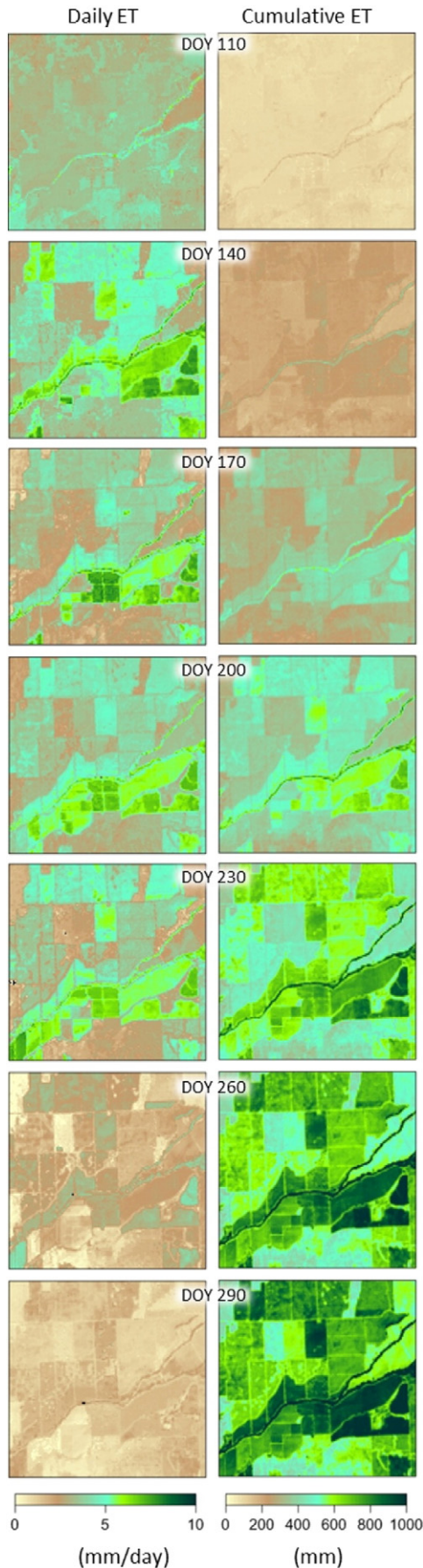
Another consideration for the early season bias is the presence of the inter-row cover crop, which is at peak greenness early in the season and is completely senesced by DOY ~160 as the vines leaf out. This transition involves a migration of transpiring vegetation from the soil surface between rows, where turbulent exchange is relatively suppressed, to the tops of the vines which are better coupled with the free atmosphere. This transition occurred later in the season in 2013 for the younger

vineyard and may require adjustment to substrate and canopy atmospheric resistance factors specific to a vineyard canopy architecture — effectively adding a "third" understory vegetation layer to the TSEB. In ongoing work, model behavior will be assessed during the 2013–2014 and 2014–2015 winter periods, and if similar bias behavior is observed, simple modifications will be developed for viticultural applications of TSEB.

A final possibility is that there may be exacerbated instrumental biases near the beginning of the experiment due to local disturbance to the soil and cover crop near the tower site, introduced during installation. There is ancillary anecdotal evidence that is consistent with this theory. Again, extension of the modeling experiment into the 2014 and 2015 field campaigns will help to determine if this was a short-term (instrumental) or persistent (model) bias.

Fig. 7 demonstrates the relative time behavior of ET fluxes (model and measurements) and soil moisture conditions during the 2013 growing season. The soil moisture data represent averages of measurements at 30, 60 and 90 cm at 3 locations near the tower in Site 1, and 2 locations in Site 2 (one set of measurements at Site 2 was non-representative due to issues with the adjacent irrigation tubing). Also shown are approximate weekly irrigation amounts, expressed in units of weekly liters per vine, included here to demonstrate the time variability in rates of water supplied through the drip lines. Given the average vine spacing within the fields, 1 l per vine translates to approximately 0.2 mm of water. Irrigation scheduling is designed to maintain relatively constant soil moisture content during the critical period of grape development, as evidenced in the soil moisture measurements in Fig. 7. In 2013, irrigation commenced in mid-June as the cover crop senesced and was suspended one or two days before harvest (around DOY 245) to prevent the harvesting machines from becoming mired in mud. Irrigation resumed post-harvest until October 4 (DOY 275).

In terms of cumulative water use, STARFM reproduced observed values derived from the EC measurements in Site 1 over the period DOY 106-245 (from first Landsat date to harvest date) within 14 mm (2% error) due to time-averaging of random daily error component and good model performance later in the season. Cumulative ET for Site 2 is more significantly overestimated at DOY 245 by about 84 mm

Fig. 8. Spatial timeseries (every 30 days) of 24-h ET (left column) and cumulative ET (right column) over a 4 × 4 km area including the two vineyard sites instrumented for GRAPEX. Individual fields are easily distinguishable as are times of higher ET (and possible irrigation).

(16%), resulting from the early season wet bias discussed above. The model predicts a lower total ET cumulative value for Site 2 than for Site 1, in accordance with the observed difference between the two fields.

4.3. Spatial patterns in evapotranspiration (ET)

Spatial patterns in the fused 30-m flux fields of daily ET over the course of the growing season are varied and complex. Fig. 8 demonstrates variability in modeled daily and cumulative ET through the study period over a 4 × 4 km box, approximating the ALEXI pixel area, including the GRAPEX vineyards near the center. Early in the season (DOY 110), ET is relatively uniformly distributed over the area while the background grasslands are still green. On DOY 140, the highest ET rates are associated with a few young vineyards in the southeast quadrant of the image — likely resulting from early irrigation applied to help establish the newly planted vines. On DOY 170, four fields of alfalfa south of the GRAPEX vineyards are highlighted. Alfalfa has a relatively high water use requirement among agricultural crops. Daily water use in the GRAPEX vineyards diminishes prior to harvest (around DOY 245 in 2013). ET variations between fields can be a result of different crop types or irrigation practices, or may relate to different soil characteristics such as texture and water holding capacity. Cumulative ET gradually increases throughout the season as well (Fig. 8, right column) but rapidly increases between DOY 230 and 260, the period covering highest maturity of vines and harvest time.

While most fields in the surrounding area are vineyards of varying levels of maturity, the four alfalfa fields directly south of the two GRAPEX field sites have a distinctly different ET signal over time. The high temporal frequency of clear-sky Landsat acquisitions over this study area (approximately every 9 days) enables the identification of when these fields (together roughly 600 by 650 m^2) were cut (between DOY 202 and 211, Fig. 9), with the ET signal showing very strongly on DOY 202 and a few days later is equivalent to background ET. Note that this scale of change (sub-MODIS pixel scale) is not likely to be robustly recovered by the Landsat/MODIS fusion process. Such localized change detection can only be accomplished with sufficient sampling at the Landsat scale.

Cumulative seasonal ET (Fig. 10) over a broader (9 × 9 km) area surrounding the GRAPEX study site demonstrates the spatial detail in water use information that can be generated using sharpened L8 TIRS imagery. Unplanted gullies in vineyards in the southeast are detectable, as is variability in the low-density residential area in the northwest corner of the image (in contrast to the dense stand of Eucalyptus trees due south). At Landsat scale, it is possible to quantify seasonal water use by crop and landcover type — again, this is not possible with MODIS.

4.4. Subfield variability in water use and yield

To better understand the reliability of sub-field variations in water use apparent at the Landsat 30-m scale, a high resolution (5 m) 24-h ET map was derived for the instrumented vineyard fields by applying DisALEXI to thermal and NDVI imagery obtained by aircraft on the day of the June 12, 2013 Landsat 8 overpass (DOY 163). The within-field ET variability at 5 m resolution (Fig. 11b) is generally spatially similar to that apparent in the 30 m resolution ET estimates (Fig. 11c), albeit with much finer detail, partially resolving the individual vine rows. The higher resolution of the aircraft imagery enables identification of distinct features. For example, an old river bed is seen in both images in the lower half of the southern field where ET is slightly higher due
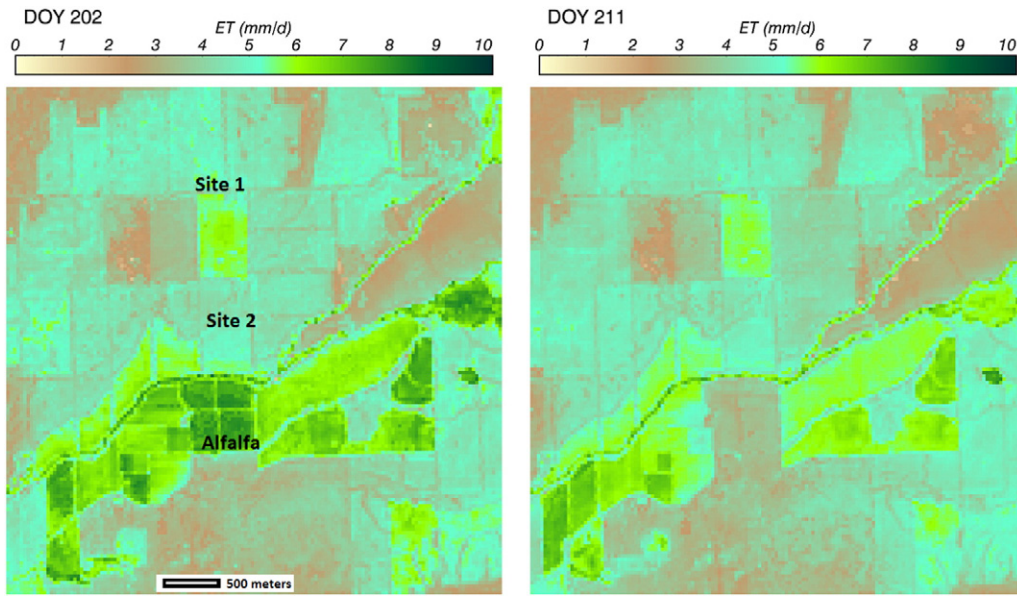
Fig. 9. Two up close snapshots of Site 1 and Site 2, as well as the alfalfa field just south of these fields. The four alfalfa fields have very high ET on day 202, but just a few days later are essentially bare due to harvesting.

to different soil characteristics. The small rectangular areas of low cumulative ET and high LST in the southern end of Site 1 (north field) are vernal pools — ephemeral ponds which are protected by state and federal law from new cultivation activities. These areas have not been planted in vines and are not irrigated. The central part of the northern field shows higher rates of ET at both scales, coinciding with a region of more vigorous vine growth. Lower ET in the upper left of the northern field is associated with soil texture discontinuities. The major soil type in the two fields is Kimball silt loam but there are small areas within the field (such as in the upper left corner of the northern field) with silt loam and gravelly loam soils which have poor to moderate water storage capacity. The area of low ET/high LST at the top middle of the northern field is associated with a house, parking area and storage sheds where equipment is kept for maintaining the fields (blanked in the aircraft image).

The aircraft imagery from DOY 163 was collected prior to the rainfall event on DOY 175 (Fig. 5). During the period DOY 180-210 when the localized enhancement in EC latent heat flux was observed at Site 1, winds were primarily from the SW – passing over the vernal pool systems, which terminate a local drainage system within that field. One possible explanation for that enhancement might be that the pools and surrounding drainages saturated during the rain event, contributing to higher evaporative losses within the tower footprint for several days as the area dried. Given that these features are classified as vernal pools, this may not be unreasonable. The L8 TIRS data at native resolution are too coarse to resolve such small scale cooling impacts on the LST field, and indeed the DMS thermal sharpening technique would erroneously impose a *higher* LST over the low NDVI area associated with the pools. A high resolution aircraft acquisition during this period would have helped to identify localized moisture enhancements within the footprint. In 2014 and 2015, GRAPEX integrated imaging using Unmanned Aerial Vehicles (UAVs), which may be easier to deploy in rapid response to episodic change events.

Within-field spatial variability in ET at 30 m resolution, both at daily and cumulative timesteps (Fig. 11c and d) shows some regions of general spatial correspondence with yield maps produced for both fields at harvest (Fig. 11a). Yield in wine grape production is carefully managed to support both wine quality and regional marketing considerations, and is not always well-correlated (and is sometimes anti-correlated) with climatic drivers. This may make year-to-year prediction of at-harvest yield difficult using remote-sensing based vegetation and

stress indicators. The ET maps at both aircraft and Landsat scale, however, do provide some information about sub-field variability in realized yield. For example, the effects of soil texture variations in the upper left corner of the north field are evident, leading to lower local yields and seasonal evaporative losses. The region of higher water use in the central part of this field resulted in higher yields in 2013. Variable rates of water application across the field, informed by high-resolution aircraft or medium resolution Landsat imagery, may serve to better homogenize production across individual fields. Research investigating multi-year yield variability in the GRAPEX fields, and correlations with anomalies in ET and vegetation index, is underway.

5. Conclusions

Performance of multi-sensor and scale data fusion approach to mapping ET using GOES, MODIS and Landsat TIR and shortwave
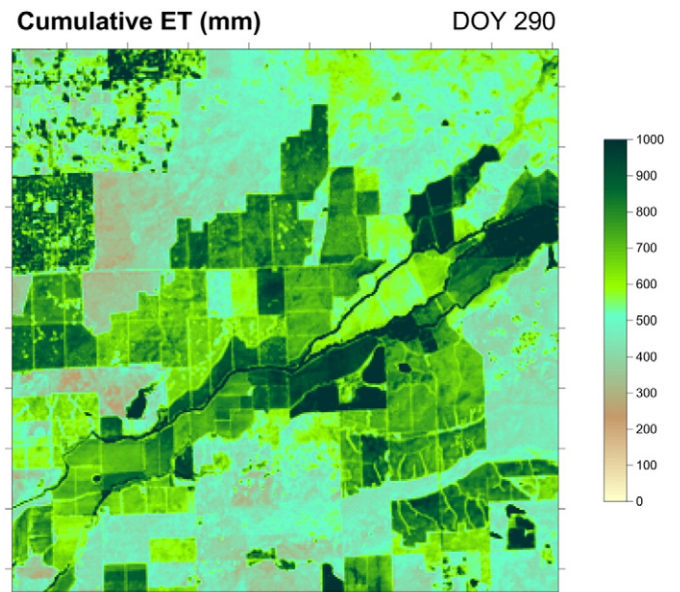

Fig. 10. Cumulative seasonal ET (mm) map (9 × 9 km) on DOY 290 surrounding the GRAPEX study.
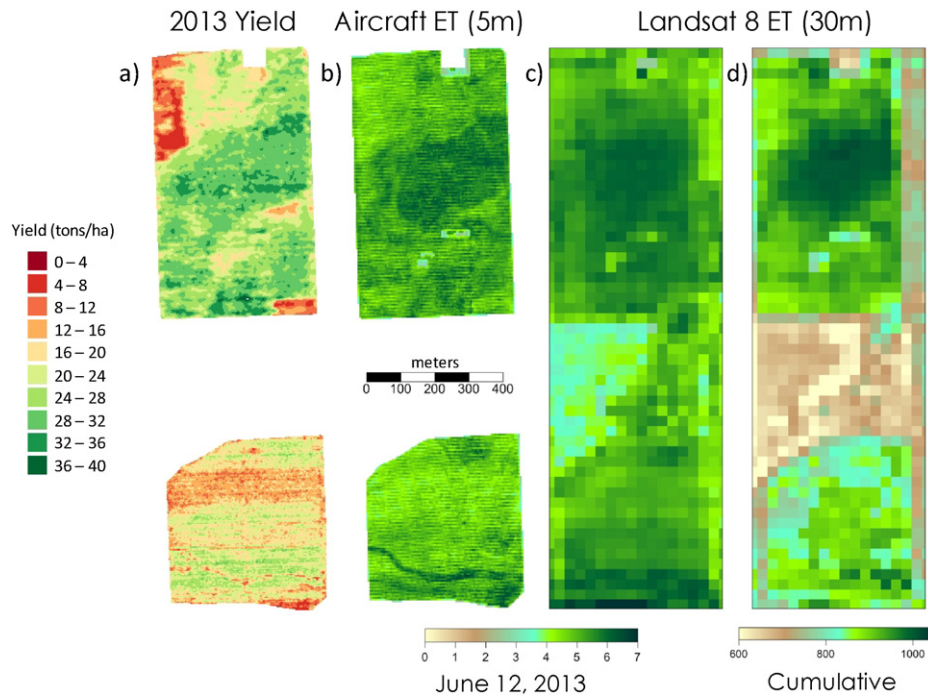
Fig. 11. Spatial distribution of a) yield (metric tons per ha) at the end of the 2013 season; b) 24-h evapotranspiration (ETd) at 5 m resolution from DisALEXI applied to aircraft imagery for DOY 163; c) 24-h evapotranspiration (ETd) at 30 m resolution from DisALEXI applied to Landsat LST for DOY 163; d) cumulative evapotranspiration (DOY 106-245) at the end of season at 30 m resolution derived from STARFM daily ET output.

imagery was assessed in an application over two vineyard sites in central California using data products from the new Landsat 8 satellite. Both temporal and spatial timeseries of ET show interesting details in water use variability within the individual fields as well as in contrast with the surrounding area. Daily ET over the 2013 growing season was retrieved at 30-m spatial resolution using a Landsat/MODIS fusion approach with percent errors of 19 and 23% in comparison with EC measurements from flux tower sites established in irrigated fields with 8 and 5-year old Pinot noir vines, respectively (Sites 1 and 2), and RMSE on the order of 1 mm d^{-1} for the full fused daily timeseries covering the growing season. In comparison, percent errors for Landsat overpass dates were 12 and 16% for Sites 1 and 2, respectively (RMSE ~0.5 mm d^{-1}), indicating some degradation in model performance for days when actual Landsat-scale TIR imagery is not available.

Cumulative ET maps from DOY 106 to 245 (date of first Landsat 8 scene to harvest) demonstrate strong variability in seasonal water use in relationship to crop type and water management strategy. Cumulative ET was predicted to within 2% for the more mature vineyard (Site 1), while in the younger vineyard site, cumulative ET was overestimated by 16% due to an early season wet bias. This overestimation may have an instrumental component, or may in part relate to issues with model parameterizations of canopy architecture relating to a between-row grass cover crop used to consume excess springtime moisture. This bias will be further investigated using data collected between the 2013, 2014 and 2015 growing seasons.

Comparison with a higher resolution (5 m) ET map generated using TIR and shortwave imagery acquired during a GRAPEX IOP indicated that much of the sub-field structure in ET apparent at Landsat-scale can be associated with real features on the ground. General spatial correspondence of fused daily and cumulative ET maps with within-field variability in at-harvest yield maps suggest potential utility for adaptive precision management of irrigation applications to homogenize grape production across fields. Combined utility for yield prediction of synchronized timeseries of daily ET (indicating water limitations) and vegetation index maps (indicating growth rate and phenological stage), both generated using STARFM, is under investigation.

Despite the observed limitations, the ET data fusion methodology described here can provide detailed information about daily and seasonal water use patterns that may not be easily acquired with other methodologies. This information, if generated operationally, can be of utility for irrigation managers at the scale of individual fields as well as for regional monitoring of water use toward allocation and conservation efforts. While decisions regarding irrigation amount and timing depend on multiple factors, such as visual appearance, measurements of leaf water potential, and other plant health measures, daily ET can provide a more comprehensive measurement of how entire field sites are faring, especially useful for large operations.

In ongoing work, the data fusion methodology is being applied over other cropping regions with different management characteristics and to forested areas as well. The ability to monitor water use effectively at field scale is significant both for viticulture, where maintaining a delicate balance of moderate water stress during the growing season is critical for wine grape production, and for other agricultural and forest production systems in regions where there are many competing water uses and limited water supply.

religion, sexual orientation, genetic information, political beliefs, reprisal, or because all or part of an individual's income is derived from any public assistance program. (Not all prohibited bases apply to all programs.) Persons with disabilities who require alternative means for communication of program information (Braille, large print, audiotape, etc.) should contact USDA's TARGET Center at (202) 720-2600 (voice and TDD). To file a complaint of discrimination, write to USDA, Director, Office of Civil Rights, 1400 Independence Avenue, S.W., Washington, D.C. 20250-9410, or call (800) 795-3272 (voice) or (202) 720-6382 (TDD). USDA is an equal opportunity provider and employer.

References

Allen, R.G., Pereira, L.S., Raes, D., & Smith, M. (1998). Crop evapotranspiration: Guidelines for computing crop water requirements. *United Nations FAO, irrigation and drainage paper. 56*, (FAO - Food and Agriculture Organization of the United Nations, 300 pp., Rome, Italy).

Allen, R.G., Tasumi, M., & Trezza, R. (2007). Satellite-based energy balance for mapping evapotranspiration with internalized calibration (METRIC) — Model. *Journal of Irrigation and Drainage Engineering, 133*, 380–394.

Anderson, M.C., Allen, R.G., Morse, A., & Kustas, W.P. (2012). Use of Landsat thermal imagery in monitoring evapotranspiration and managing water resources. *Remote Sensing of Environment, 122*, 50–65.

Anderson, M.C., Kustas, W.P., Alfieri, J.G., Gao, F., Hain, C., Prueger, J.H., ... Chavez, J.L. (2012). Mapping daily evapotranspiration at Landsat spatial scales during the BEAREX'08 field campaign. *Advances in Water Resources, 50*, 162–177.

Anderson, M.C., Kustas, W.P., Norman, J.M., Hain, C.R., Mecikalski, J.R., Schultz, L., ... Gao, F. (2011). Mapping daily evapotranspiration at field to continental scales using geostationary and polar orbiting satellite imagery. *Hydrology and Earth System Sciences, 15*, 223–239.

Anderson, M.C., Neale, C.M.U., Li, F., Norman, J.M., Kustas, W.P., Jayanthi, H., & Chavez, J. (2004). Upscaling ground observations of vegetation water content, canopy height, and leaf area index during SMEX02 during aircraft and Landsat imagery. *Remote Sensing of Environment, 92*, 447–464.

Anderson, M.C., Norman, J.M., Diak, G.R., Kustas, W.P., & Mecikalski, J.R. (1997). A two-source time-integrated model for estimating surface fluxes using thermal infrared remote sensing. *Remote Sensing of Environment, 60*, 195–216.

Anderson, M.C., Norman, J.M., Kustas, W.P., Li, F., Prueger, J.H., & Mecikalski, J.M. (2005). Effects of vegetation clumping on two-source model estimates of surface energy fluxes from an agricultural landscape during SMACEX. *Journal of Hydrometeorology, 6*, 892–909.

Anderson, M.C., Norman, J.M., Kustas, W.P., Li, F., Prueger, J.H., & Mecikalski, J.R. (2007). A climatological study of evapotranspiration and moisture stress across the continental United States: 1. Model formulation. *Journal of Geophysical Research, 112*, D11112.

Anderson, M.C., Norman, J.M., Mecikalski, J.R., Torn, R.D., Kustas, W.P., & Basara, J.B. (2004). A multi-scale remote sensing model for disaggregating regional flues to micrometeorological scales. *Journal of Hydrometeorology, 5*, 343–363.

Bastiaanssen, W.G.M., Menenti, M., Feddes, R.A., & Holtslag, A.A.M. (1998). A remote sensing surface energy balance algorithm for land (SEBAL): 1. Formulation. *Journal of Hydrology, 212-213*, 198–212.

Berk, A., Bernstein, L.S., & Robertson, D.C. (1989). *MODTRAN: A moderate resolution model for LOWTRAN 7. GL-TR-89-0122*. Bedford, MA: Air Force Geophysics Lab, 38.

Bramley, R.G.V., & Williams, S.K. (2001). *A protocol for the construction of yield maps from data collected using commercially available grape yield monitors*. Adelaide, S.A.: Cooperative Research Centre for Viticulture.

Brutsaert, W. (1982). *Evaporation into the atmosphere*. Dordrecht, The Netherlands: D. Reidel 299 pp.

California Department of Food and Agriculture, & USDA National Agricultural Statistics Service (2014). California grape acreage report 2014 crop. Available on-line http://www.nass.usda.gov/Statistics_by_State/California/Publications/Fruits_and_Nuts/201503grpac.pdf

Cammalleri, C., Anderson, M.C., & Kustas, W.P. (2014). Upscaling of evapotranspiration fluxes from instantaneous to daytime scales for thermal remote sensing applications. *Hydrology and Earth System Sciences, 18*, 1885–1894.

Cammalleri, C., Anderson, M.C., Gao, F., Hain, C.R., & Kustas, W.P. (2014). Mapping daily Evapotranspiration at field scales over rainfed and irrigated agricultural areas using remote sensing data fusion. *Agricultural and Forest Meteorology, 186*, 1–11.

Cammalleri, C., Anderson, M.C., Gao, F., Hain, C.R., & Kustas, W.P. (2013). A data fusion approach for mapping daily Evapotranspiration at field scale. *Water Resources Research, 49(8)*, 4672–4686.

Chaves, M.M., Santos, C.R., Ortuno, M.F., Rodrigues, M.L., Lopes, C.M., Maroco, J.P., & Pereira, J.S. (2007). Deficit irrigation in grapevine improves water-use efficiency while controlling vigour and production quality. *Annals of Applied Biology, 150*, 237–252.

Chavez, J.L., Neale, C.M.U., Hipps, L.E., Prueger, J.H., & Kustas, W.P. (2005). Comparing aircraft based remotely sensed energy balance fluxes with eddy covariance tower data using heat flux source area functions. *Journal of Hydrometeorology, 6*, 923–940.

Cosgrove, B.A., et al. (2003). Real-time and retrospective forcing in the North American Land Data Assimilation System (NLDAS) project. *Journal of Geophysical Research, 108*, D228842http://dx.doi.org/10.1029/2002JD003118.2003.

Evett, S.R., Kustas, W.P., Gowda, P.H., Anderson, M.C., Prueger, J.H., & Howell, T.A. (2012). Overview of the Bushland Evapotranspiration and Agricultural Remote sensing EXperiment 2008 (BEAREX08): A field experiment evaluating methods for quantifying ET at multiple scales. *Advances in Water Resources, 50*, 4–19.

French, A.N., Jacob, F., Anderson, M.C., Kustas, W.P., Timmermans, W., Gieske, A., ... Brunsell, N. (2005). Surface energy fluxes with the Advanced Spaceborne Thermal Emission and Reflection radiometer (ASTER) at the Iowa 2002 SMACEX site (USA). *Remote Sensing of Environment, 99(1–2)*, 55–65.

Fry, J., Xian, G., Jin, S., Dewitz, J., Homer, C., Yang, L., ... Wickham, J. (2011). Completion of the 2006 national land cover database for the conterminous United States. *Photogrammetric Engineering and Remote Sensing, 77(9)*, 858–864.

Gao, F., Anderson, M.C., Kustas, W.P., & Wang, Y. (2012). Simple method for retrieving leaf area index from Landsat using MODIS leaf area index products as reference. *Journal of Applied Remote Sensing, 6(1)*, 063554.

Gao, F., Kustas, W.P., & Anderson, M.C. (2012). A data mining approach for sharpening thermal satellite imagery over land. *Remote Sensing, 4*, 3287–3319.

Gao, F., Masek, J., Schwaller, M., & Hall, F. (2006). On the blending of the Landsat and MODIS surface reflectance: Predicting daily Landsat surface reflectance. *IEEE Transactions on Geoscience and Remote Sensing, 44*, 2207–2218.

Gao, F., Morisette, J. T., Wolfe, R. E., Ederer, G., Pedelty, J., Masuoka, E., ... Nightingale, J. (2008). An algorithm to produce temporally and spatially continuous MODIS-LAI time series. *Geoscience and Remote Sensing Letters, IEEE, 5(1)*, 60–64.

Hain, C.R., Crow, W.T., Anderson, M.C., & Yilmaz, M.T. (2014). Diagnosing neglected soil moisture source/sink processes via a thermal infrared-based two-source energy balance model. *Journal of Hydrometeorology* (under review).

Hansen, M.C., DeFries, R.S., Townshend, J.R.G., & Sohlberg, R. (2000). Global land cover classification at 1 km spatial resolution using a classification tree approach. *International Journal of Remote Sensing, 21*, 1331–1364.

Hsieh, C.I., Katul, G., & Chi, T. (2000). An approximate analytical model for footprint estimation of scalar fluxes in thermally stratified atmospheric flows. *Advances in Water Resources, 23*, 765–772.

Huete, A., Justice, C., & Leeuwen, W.V. (2014). MODIS vegetation index — MOD13A2. *NASA land processes distributed active archive center (LP DAAC)*. USGS/Earth Resources Observation and Science (EROS) Center: Sioux Falls, South Dakota.

Jedlovec, G.J., Haines, S.L., & LaFontaine, F.J. (2008). Spatial and temporal varying thresholds for cloud detection in GOES imager. *IEEE Geoscience and Remote Sensing Society, 46*, 1705–1717.

Jönsson, P., & Eklundh, L. (2004). TIMESAT — A program for analyzing time-series of satellite sensor data. *Computers and Geosciences, 30*, 833–845.

Kaimal, J.C., & Finnigan, J.J. (1994). *Atmospheric boundary layer flows, their structure and measurement*. New York: Oxford University Press (289 pp.).

Kustas, W.P., Norman, J.M., Anderson, M.C., & French, A.N. (2003). Estimating subpixel surface temperatures and energy fluxes from the vegetation index-radiometric temperature relationship. *Remote Sensing of Environment, 85*, 429–440.

Kustas, W.P., & Norman, J.M. (1999). Evaluation of soil and vegetation heat flux predictions using a simple two-source model with radiometric temperatures for partial canopy cover. *Agricultural and Forest Meteorology, 94*, 13–29.

Li, F., Jackson, T.J., Kustas, W.P., Schmugge, T.J., French, A.N., Cosh, M.H., & Bindlish, R. (2004). Deriving land surface temperature from Landsat 5 and 7 during SMEX02/SMACEX. *Remote Sensing of Environment, 92*, 521–534.

Li, F., Kustas, W.P., Anderson, M.C., Prueger, J.H., & Scott, R.L. (2008). Effect of remote sensing spatial resolution on interpreting tower-based flux observations. *Remote Sensing of Environment, 112*, 337–349.

Liang, S. (2000). Narrowband to broadband conversions of land surface albedo I: Algorithms. *Remote Sensing of Environment, 76*, 213–238.

Masek, J.G., Vermote, E.F., Saleous, N.E., Wolfe, R.E., Hall, F.G., Huemmrich, K.F., ... Lim, T.-K. (2006). A Landsat surface reflectance dataset for North America, 1990–2000. *IEEE Geoscience and Remote Sensing Letters, 3*, 68–72.

Massman, W.J., & Lee, X. (2002). Eddy covariance flux corrections and uncertainties in long term studies of carbon and energy exchanges. *Agricultural and Forest Meteorology, 113*, 121–144.

McNaughton, K.G., & Spriggs, T.W. (1986). A mixed-layer model for regional evaporation. *Boundary-Layer Meteorology, 34*, 243–262.

Mesinger, F., et al. (2006). North American regional reanalysis. *Bulletin of the American Meteorological Society, 87*, 343–360. http://dx.doi.org/10.1175/BAMS-87-3-343.

Montes, C., Lhomme, J.-P., Demarty, J., Prevot, L., & Jacob, F. (2014). A three-source SVAT modeling of evaporation: Application to the seasonal dynamics of a grassed vineyard. *Agricultural and Forest Meteorology, 191*, 64–80.

Moody, E.G., King, M.D., Platnick, S., Schaaf, C.B., & Gao, F. (2005). Spatially complete global spectral surface albedos: Value-added datasets derived from Terra MODIS land products. *IEEE Transactions on Geoscience and Remote Sensing, 43*, 144–158.

Moussa, R., Chahinian, N., & Bocquillon, C. (2007). Distributed hydrological modelling of a Mediterranean mountainous catchment — Model construction and multi-site validation. *Journal of Hydrology, 337*, 35–51.

Myneni, R. (2014). *4-day MODIS LAI/FPAR — MCD15A3*. Sioux Falls, South Dakota: NASA Land Processes Distributed Active Archive Center (LP DAAC), USGS/Earth Resources Observation and Science (EROS) Center.

Neale, C.M.U., Geli, H., Kustas, W.P., Alfieri, J.G., Gowda, P.H., Evett, S.R., ... Howell, T.A. (2012). Soil water content estimation using a remote sensing based hybrid evapotranspiration modeling approach. *Advances in Water Resources, 50*, 152–161.

Norman, J.M., Anderson, M.C., Kustas, W.P., French, A.N., Mecikalski, J., Torn, R., ... Tanner, B.C.W. (2003). Remote sensing of surface energy fluxes at 101-m pixel resolutions. *Water Resources Research, 39*http://dx.doi.org/10.1029/2002WR001775.

Norman, J.M., Kustas, W.P., & Humes, K.S. (1995). A two-source approach for estimating soil and vegetation energy fluxes from observations of directional radiometric surface temperatures. *Agricultural and Forest Meteorology, 77*, 263–293.

Price, J.C. (1983). Estimating surface temperatures from satellite thermal infrared data. A simple formulation for the atmospheric effect. *Remote Sensing of Environment, 13*, 353–361.

Prueger, J.H., Hatfield, J.L., Kustas, W.P., Hipps, L.E., MacPherson, J.I., & Parkin, T.B. (2005). Tower and aircraft eddy covariance measurements of water vapor, energy and carbon dioxide fluxes during SMACEX. *Journal of Hydrometeorology, 6*, 954–960.

Riou, C., Pieri, P., & Le Clech, B. (1994). Consommation d'eau de la vigne en conditions hydriques non limitantes. Formulation simplifies de la transpiration. *Vitis, 33*, 109–115.

Riou, C., Valancogne, C., & Pieri, P. (1989). Un modele simple d'interception du rayonnement solaire par la vigne — Verification experimentale. *Agronomie, 9*, 441–450.

Robinson, J. (Ed.). (2006). *The Oxford companion to wine* (pp. 840) (3rd ed.). Oxford University Press.

Su, Z. (2002). The surface energy balance system (SEBS) for estimation of the turbulent heat fluxes. *Hydrology and Earth Sciences, 6*, 85–99.

Teixeira, A. d. C., Bastiaanssen, W.G.M., & Bassoi, L.H. (2007). Crop water parameters of irrigated wine and table grapes to support water productivity analysis in the Sao Francisco river basin, Brazil. *Agricultural Water Management, 94*, 31–42.

Wan, Z. (2014). *MODIS land surface temperature product — MOD11_L2 V005.* Sioux Falls, South Dakota: NASA Land Processes Distributed Active Archive Center (LP DAAC), USGS/Earth Resources Observation and Science (EROS) Center.

Webb, E.K., Pearman, G.I., & Leuning, R. (1980). Correction of flux measurements for density effects due to heat and water vapor transfer. *Quarterly Journal of the Royal Meteorological Society, 106*, 85–100.

Williams, L.E., Grimes, D.W., & Phene, C.J. (2010). The effects of applied water at various fractions of measured evapotranspiration on reproductive growth and water productivity of Thompson Seedless. *Irrigation Science, 28*, 233–243.

Williams, L.E. (2001). Irrigation of winegrapes. *Practical Winery and Vineyard Journal, November/December 2001* Available on-line http://www.practicalwinery.com/novdec01p42.htm

Willmott, C.J. (1982). Some comments on the evaluation of model performance. *Bulletin of the American Meteorological Society, 63*, 1309–1313.

Willmott, C.J., & Matsuura, K. (2005). Advantages of the mean absolute error (MAE) over the root mean square error (RMSE) in assessing average model performance. *Climate Research, 30*, 79–82.

Zhu, Z., Wang, S., & Woodcock, C.E. (2015). Improvement and expansion of the Fmask algorithm: cloud, cloud shadow, and snow detection for Landsats 4–7, 8, and Sentinel 2 images. *Remote Sensing of Environment, 159*, 269–277.